Coastal Engineering 169 (2021) 103973

Contents lists available at ScienceDirect

Coastal Engineering

journal homepage: www.elsevier.com/locate/coastaleng

Wave overtopping due to harbour resonance

Nikolaos Maravelakis [a,*], Nikos Kalligeris [b], Patrick J. Lynett [c], Vassilios L. Skanavis [d], Costas E. Synolakis [c,d]

[a] School of Environmental Engineering, Technical University of Crete, Polytechneioupolis, 73100 Chania, Greece
[b] Institute of Geodynamics, National Observatory of Athens, 11851 Athens, Greece
[c] Department of Civil and Environmental Engineering, University of Southern California, Los Angeles, CA, 90089, USA
[d] Research Centre for Atmospheric Physics and Climatology, Academy of Athens, Athens 10680, Greece

ARTICLE INFO

Keywords:
Wave overtopping
Numerical modelling
Boussinesq
Harbour resonance
Field measurements

ABSTRACT

Harbour resonance and its contribution to wave overtopping are examined for a small irregular-shaped harbour in the eastern Mediterranean. Offshore wave measurements are used to determine the incident wave conditions during storm events. Resonant periods of the harbour basin are identified through in situ measurements at four different deployment locations during multiple storm events. Numerical simulations using a Boussinesq-type model and an idealised offshore spectrum yielded similar resonant frequencies to the field measurements and allowed us to visualise the corresponding resonant modes. Wave overtopping along the vertical docks of the harbour is inferred by combining numerical time series of free surface elevation with EurOtop formulae. Two approaches to estimate wave overtopping rates are examined and compared: a novel approach considering wave energy in the sea-swell frequency range and varying the freeboard through time series in the infragravity frequency range, and the conventional method that considers spectral parameters along the entire frequency range. The novel approach provides an estimate for the contribution of harbour resonance to wave overtopping considering that infragravity wave energy inside the basin is mainly resonance-driven.

1. Introduction

Coastal areas are constantly interacting with the sea, and are under anthropogenic pressures as well as climate change-induced sea-level rise. Rising seas are likely to affect harbour operations and further work is required to clearly address the challenges of these implications (Asariotis et al., 2018), such as site-specific studies used to infer the future impact of climate change on port operations (e.g., Sierra et al., 2017; Abdelhafez et al., 2021; Camus et al., 2019). Wave overtopping is among the processes contributing to physical coastal impacts such as inundation, erosion, and coastal flooding (Wong et al., 2014). Overtopping discharges and consequently flooding are expected to intensify due to rising sea levels (Chini and Stansby, 2012; Gallien et al., 2014; Vitousek et al., 2017; Vousdoukas et al., 2018; Xie et al., 2019). Globally aggregated annual overtopping hours are projected to increase up to 50 times by the end of the 21st century under the worst case climate change scenario (Almar et al., 2021). Hence, enhanced efforts to better understand the underlying physical processes contributing to wave overtopping at coastal infrastructures are paramount.

The penetration of infragravity (IG) waves in harbours is well documented for enhancing wave agitation (Okihiro and Guza, 1996; McComb et al., 2005; Thotagamuwage and Pattiaratchi, 2014), especially for harbours with entrances exposed to shallow foreshores. These motions interrupt berthing operations and can cause overtopping along the docks in cases of poorly sheltered basins (Gierlevsen et al., 2001; McComb et al., 2009; Thotagamuwage and Pattiaratchi, 2014; Maravelakis et al., 2016). IG waves have periods ranging between 25 and 600 s (Rabinovich, 2009) and are generated through non-linear interactions of wind-generated waves (Longuet-Higgins and Stewart, 1962; Baldock and Huntley, 2002; Battjes et al., 2004). Existing analytical and experimental results have given insight on the contribution of incoming short period waves to IG period oscillations in harbour basins. Bowers (1977) concluded that bound waves trapped in swell-wave groups and travelling towards the shoreline at the group velocity directly excite natural oscillation periods, leading to resonance. Free long waves, released through breaking, can also excite low-frequency oscillations, including the resonant modes of a harbour basin (De Girolamo, 1996; Mei and Agnon, 1989; Wu and Liu, 1990; Gao et al., 2016).

In two landmark papers, Okihiro et al. (1993) and Okihiro and Guza (1996) recognised ocean swells as the primary energy source

* Corresponding author.
E-mail addresses: nmaravelakis@isc.tuc.gr (N. Maravelakis), nkalligeris@noa.gr (N. Kalligeris), lynett@usc.edu (P.J. Lynett), skanavis@usc.edu (V.L. Skanavis), costas@usc.edu (C.E. Synolakis).

https://doi.org/10.1016/j.coastaleng.2021.103973
Received 3 January 2021; Received in revised form 9 July 2021; Accepted 4 August 2021
Available online 14 August 2021

for harbour seiches at frequencies above 0.002 Hz, using field measurements at Barbers Point and Kahului harbours of Hawaii, and at Oceanside harbour in California. Morison and Imberger (1992) found that resonance in Esperance harbour, Western Australia was a result of incoming swells of periods between 15–25 s and other longer oscillations (> 40 s), while López et al. (2012) found that long-period oscillations (0.7 mHz < f < 2.5 mHz) in the Port of Ferrol, Spain were strongly correlated with offshore swell energy. However, IG generation has also been observed under storm conditions (Holman et al., 1978; Nakamura and Katoh, 1993; Jeong et al., 1997). Thotagamuwage and Pattiaratchi (2014) concluded that oscillations in a small marina in SW Australia were generated by offshore swell waves and they were further amplified during storm events.

Numerical simulations have been proven useful for studying the contribution of IG waves to harbour resonance. Harkins and Briggs (1995) numerically found more infragravity wave energy inside Barbers Point harbour from narrow banded incident spectra than from broad banded spectra, which was confirmed through field and laboratory data. Long wave penetration and wave amplification has been studied in Marina di Carrara, Italy using Mild Slope Equation (MSE) and Boussinesq-type (BT) numerical models (Bellotti and Franco, 2011; Bellotti et al., 2012; Guerrini et al., 2014; Cuomo and Guza, 2017). Results were validated through extensive field measurements and was found that long waves in the range 0.003–0.3 Hz are forced by short incoming waves (Bellotti and Franco, 2011). Low frequency oscillations in the Hambanota port, Sri Lanka, were investigated during the southwest monsoon of 2019 in the Indian Ocean, combining field measurements and numerical simulations based on an extended MSE model (Dong et al., 2020b). Analysis of simulation results and measurements resulted in the identification of the port's natural frequencies, while field measurements revealed stronger correlation of the lower frequency oscillations in the port with lower frequency incident energy offshore. Kofoed-Hansen et al. (2005) performed numerical simulations using a BT model for Torsminde harbour, Denmark, and the Port of Long Beach in California, and attributed the generation of low-frequency energy forcing harbour resonance to the non-linear interaction of short waves. Recently, Kwak et al. (2020) and Leys et al. (2018) combined field measurements with BT model simulation results to study the effect of harbour basin geometry and design to wave amplification due to resonance, and proposed solutions to mitigate the problem for small craft harbours on the Atlantic coast of Canada and Mukho harbour, Korea, respectively. Similar studies focusing on solutions to reduce harbour oscillations have also been conducted by Gierlevsen et al. (2001) and McComb et al. (2009). In addition to suggesting engineering solutions to already problematic situations, Kofoed-Hansen et al. (2001) have suggested the use of BT-models for the initial design of marinas and the identification of oscillations modes.

Taking into account the necessity to reduce computational time for forecasting applications (Troch et al., 2021; André et al., 2021), Artificial Neural Networks (ANN) have also been applied for the prediction of long wave heights in ports and harbours, using field measurements and numerical results from BT models in the training procedure of the neural networks (López and Iglesias, 2013; Zheng et al., 2020; Dong et al., 2020b). Lately, considerable research has been focused on the transient resonance inside harbours triggered by long period waves, such as tsunamis, using numerical simulations validated by physical experiments (Dong et al., 2020a; Gao et al., 2020; Ma et al., 2021; Zheng et al., 2021).

In terms of the contribution of IG waves to wave runup and overtopping, the release of IG waves in the surf zone and their contribution to the swash has been studied by Raubenheimer et al. (1996) and Guza and Thornton (1982), respectively. Ruessink et al. (1998) have found that, for the dissipative beaches of the Dutch coast, IG energy dominates the swash, while McCall et al. (2014) and Baumann et al. (2017) have shown for reflective and dissipative beaches, respectively, that under low-freeboard conditions large wave overtopping events are mainly driven by IG waves.

The EurOtop (2018) manual recommends using the spectral energy wave period $T_{m-1,0} = m_{-1}/m_0$, where m_n are the spectral moments defined as $m_n = \int_0^\infty S f^n df$, where f is the period and $S(f)$ is the spectral density. Using the $T_{m-1,0}$ spectral period ensures that the lower frequency energy range is included in estimations of overtopping rates. Hofland et al. (2017) derived a $T_{m-1,0}$ prediction formula for shallow foreshores, and showed that $T_{m-1,0}$ can increase up to eight times for extremely shallow foreshores. Oosterlo et al. (2018) found that infragravity waves need to be considered in wave overtopping studies as they were found to have a large contribution to the probability of failure of dikes, and suggested that further research was needed on this topic.

Compared to the incident wave conditions impacting the open coast, the wave environment inside a harbour is far more complicated during storm events. Multiple incident wave directions inside the basin are generated due to refraction and reflections off vertical structures. As is, estimation of overtopping rates in empirical formulae is based on incident wave heights (e.g. EurOtop, 2018), yet in harbours, reflections might double the wave heights impacting the quays. Harbour resonance leads to wave amplification at the basin's natural oscillation frequencies, whose spatial distribution corresponds to the resonant modes. The modes, and by extension the incident wave conditions along the docks are multidirectional, and thus it becomes challenging to define incident wave directions to be used with empirical formulae (e.g. EurOtop, 2018). However, harbour resonance can play an important role in wave overtopping along quays (Gensen, 2017), and it should not be neglected. To overcome the complexity of wave overtopping inside harbour basins, Nicolai et al. (2016) simply formulated the influence of wave overtopping by adding a static 0.3 m to the water level to estimate the flooding risk along quays of Rotterdam harbour.

In an effort to better understand the contribution of IG waves in overtopping, this study examines the oscillation modes that resonate in the Venetian harbour of Chania, Greece, in storm conditions. We set out to quantify the physical problem by identifying the local wave climate and better understanding the effects of resonance for the Venetian harbour. An extensive field campaign over a time period of nine years, resulted in a dataset of measured waves offshore and inside the harbour for numerous storm events. The locations where measurements were made inside the harbour were selected with the BT-model (COULWAVE, Lynett, 2002). The numerical and field results on resonant modes are analysed and compared. Results from the numerical simulations are used for the estimation of overtopping rates along the docks of the western basin using empirical formulas from EurOtop (2018), and, finally, we examine the contribution of infragravity waves to overtopping rates.

2. Study site

The harbour of Chania is located on the northwestern coast of the island of Crete (inset of Fig. 1a). The harbour was constructed by the Venetians in the 14th century, on a natural rocky shelter. Nowadays, the harbour is an archaeological and recreational attraction in Crete. Hotels, cafes and restaurants occupy the docks.

The harbour is divided into a western and an eastern basin (Fig. 1a). The western basin is used by a limited number of recreational boats during the summer period, while sailboats and fishing boats make use of the sheltered eastern basin throughout the year. The harbour entrance is located at the western basin, while a ~ 4 m wide rectangular culvert close to the eastern edge of the harbour's breakwater (label 2, Fig. 1a) allows for the circulation and renewal of sea water between the basins and the open sea. Another distinctive feature is the canyon out of the entrance which is an artificial approaching channel dredged in different phases in the past to deepen the shallow waters surrounding the harbour and facilitate the safe entrance of ships. Its depth is about

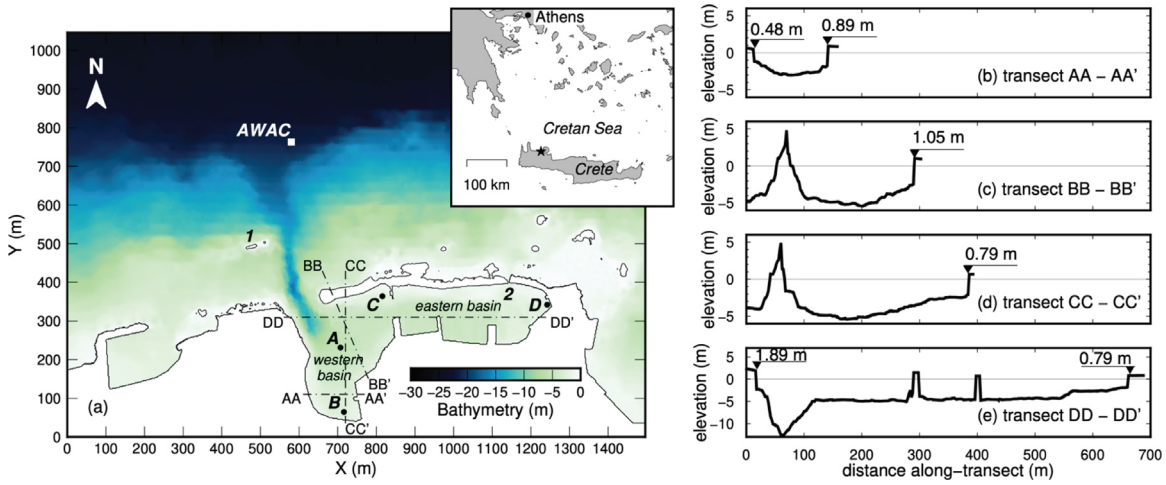

Fig. 1. (a) Bathymetry of the study area and instrument deployment locations (AWAC, A, B, C, D); label 1 shows the location of the low-crested offshore breakwater, and label 2 designates the culvert in the eastern harbour basin. The study area location is shown with the black star in the inset figure. (b–e) Transects of the relief grid (bathymetry/topography, 2 m cell size) across the harbour basins; plan view of each section is provided in (a). (For interpretation of the references to colour in this figure legend, the reader is referred to the web version of this article.)

16 m at its deepest point just north of the entrance. Its orientation coincides with the direction of incident waves during storm events and as a result waves entering the channel refract out of it and propagate to the harbour's entrance with reduced height and energy (Zwamborn and Grieve, 1975; Dusseljee et al., 2014).

A vexing issue with the harbour is the exposed and insufficiently protected entrance facing a ~ 180 km north fetch. During winter storm events, the western basin experiences up to 2 m waves and significant wave overtopping volumes. The western and southern docks of the western basin often flood (Fig. 2b–c), while plunging waves impact violently the dock facing the entrance (Fig. 2e), with up-rushing water jets overtopping it. The only protection is provided by a low-crested offshore breakwater (label 1, Fig. 1a) which was partially fulfilled in the early 90's. The partial fulfilment has led to successive failures of the structure and as a result it does not provide the protection it was designed for.

3. Field measurements and harbour observations

3.1. Field data collection

Fig. 1a shows the instrument deployment locations. The offshore wave climate is being measured using the acoustic AWAC 600 kHz directional wave system (Nortek, 2021). The instrument makes use of four acoustic transducers, one in the centre facing the water surface and three others on the sides, oriented 25° off the vertical axis. The transducer in the centre directly measures the changes in sea surface elevation through the Acoustic Surface Tracking (AST) method, while the other three measure wave-generated orbital velocities from which the directional parameters are derived. The instrument deployed at ~ 23 depth (see Fig. 1a), can accurately measure waves as short as 1 s period and 1.47 m wavelength through the AST method. Estimates of directional parameters at these depths are reliable for waves with peak periods greater than 3 s (Nortek, 2018). The AWAC is mounted on a tripod steel base stabilized in place by the weight of an enclosed deep-cycle battery mounted at the bottom of the tripod. The wave measurements are scheduled at a rate of 2 Hz for 1200 s/h, starting on October 6th, 2011. The data collection has been continuous to this day, apart from two minor and three major data gaps which represent ~ 28% of the whole dataset. The recorded time series are used to obtain the fundamental statistical and spectral wave parameters to characterize the sea state, using the zero down crossing method in the time-domain and FFT (Fast Fourier Transform) in the frequency-domain.

Inside the harbour basin, four locations were chosen to collect free surface elevation measurements (see deployment locations in Fig. 1a). Deployment location A is in the centre of the western basin at ~ 5 m depth. Locations B and C correspond to the southern and northern parts of the western basin, respectively, deployed at depths of ~2 m. Deployment location D was located at the eastern-most point of the harbour, also at ~ 2 m depth. The measurements were collected simultaneously in three out of the four deployment locations using one TWR-2050 and two RBR-Duet pressure gauges, the sensors being deployed at different locations during storm events. Sampling rate was set at 1 Hz recording for 4096 s with a 2 s gap in-between successive recordings.

3.2. Description of offshore wave climate

Results from the statistical analysis of the offshore measurements are given in the joint distribution table of significant wave height, $H_{1/3}$ and significant wave period $T_{1/3}$ (Table 1). The data covers the period from October 6, 2011 until the 20th of August, 2020. Calm sea state values ($H_{1/3} < 0.25$ m) represent ~ 18%. $H_{1/3}$ values of intense storm events ($H_{1/3} > 4$ m) are observed at significant wave periods between 8 and 11 s, while significant wave heights (2.5 m < $H_{1/3}$ < 4 m) in common storm conditions have significant wave periods in the range of 6–10 s. Predominant directions of incident waves in the study area are from NW to N (60%) with the storm waves coming mostly from NNW and N directions. Throughout the monitoring period, the most severe storms were recorded in the winter months of 2015, 2019 and 2020, with significant wave heights exceeding 4.5 m in eight storm events. The maximum $H_{1/3} = 6.06$ m and $H_{max} = 9.89$ m values were recorded on January 6th, 2020, with $T_{1/3} = 9.96$ s.

The tidal range in the Mediterranean Sea is of the order of centimetres. Long-term water level readings for the Venetian harbour of Chania are not available, with the nearest permanent station being the tide gauge in Souda Bay (~ 7 km SE of Chania), operated by the Hellenic Hydrographic Service.

Tidal constituents for the study area of Chania were obtained from the AWAC water level recordings of each deployment (hourly average water level using 20 min samples) using the T_Tide tidal harmonic analysis tool (Pawlowicz et al., 2002). Since AWAC deployments ranged between 4–6 months, only the diurnal and semi-diurnal tidal constituents were estimated. The diurnal (O_1, K_1, P_1) and semi-diurnal (M_2, S_2, N_2, K_2) tidal constituents sum up to a tidal range of ±2.3 cm, a typical low tidal range of the Mediterranean sea (Tsimplis et al., 1995).

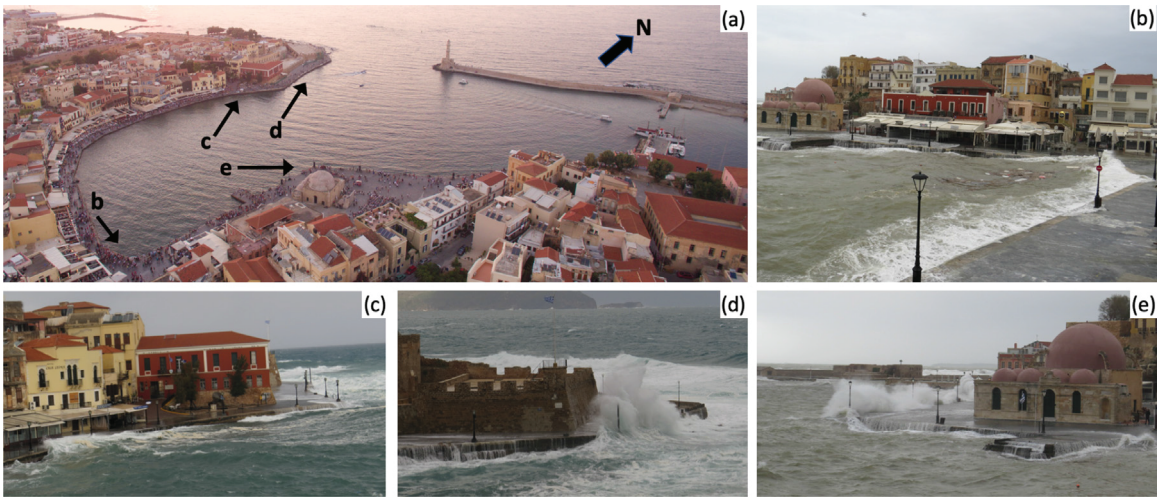

Fig. 2. (a) Aerial picture of the western harbour basin (Credit: Konstantinos Gdontakis). (b–e) Wave overtopping pictures along western-basin docks under storm conditions: (b–c) green wave overtopping at the southern-most and the western dock of the western basin, respectively; (d–e) wave overtopping under impulsive conditions at the NW and SW docks of the western basin, respectively. Arrows in (a) indicate the locations pictured in (b–e). (For interpretation of the references to colour in this figure legend, the reader is referred to the web version of this article.)

Table 1
Joint distribution table of $H_{1/3}$ and $T_{1/3}$ for the offshore wave climate in the study area, derived from field measurements collected during the time period between October 6th, 2011–August 20th, 2020. The prevailing classes of $H_{1/3}$ and $T_{1/3}$ pairs are in bold.

$H_{1/3}$ (m)	$T_{1/3}$ (s)										Sum (%)
	0–3	3–4	4–5	5–6	6–7	7–8	8–9	9–10	10–11	11–12	
NoData											**27.64**
<0.25	2.87	**9.65**	4.38	1.01	0.13	0.01	0.003	0.004	0.001	0.003	**18.07**
0.25-0.5	2.50	**10.08**	8.88	1.49	0.46	0.05	0.00	0.00	0.00	0.00	**23.46**
0.5-1.0	0.12	3.84	**9.90**	5.49	0.22	0.05	0.004	0.00	0.00	0.00	**19.61**
1.0-1.5	0.00	0.003	0.51	**4.11**	1.19	0.01	0.001	0.001	0.00	0.00	**5.82**
1.5–2.0	0.00	0.00	0.01	0.40	**1.99**	0.12	0.001	0.00	0.00	0.00	**2.53**
2.0–2.5	0.00	0.00	0.00	0.01	**0.81**	0.47	0.01	0.00	0.00	0.00	**1.30**
2.5–3.0	0.00	0.00	0.00	0.00	0.08	**0.63**	0.05	0.00	0.00	0.00	**0.76**
3.0–3.5	0.00	0.00	0.00	0.00	0.00	**0.23**	0.15	0.004	0.00	0.00	**0.38**
3.5-4.0	0.00	0.00	0.00	0.00	0.00	0.02	**0.19**	0.01	0.00	0.00	**0.22**
4.0–4.5	0.00	0.00	0.00	0.00	0.00	0.00	**0.10**	0.03	0.00	0.00	**0.13**
4.5–5.0	0.00	0.00	0.00	0.00	0.00	0.00	0.01	**0.04**	0.00	0.00	**0.05**
5.0–5.5	0.00	0.00	0.00	0.00	0.00	0.00	0.00	**0.01**	0.00	0.00	**0.01**
5.5–6.0	0.00	0.00	0.00	0.00	0.00	0.00	0.00	**0.003**	**0.003**	0.00	**0.005**
6.0–6.5	0.00	0.00	0.00	0.00	0.00	0.00	0.00	**0.001**	0.00	0.00	**0.001**
Sum (%)	**5.49**	**23.57**	**23.69**	**12.50**	**4.88**	**1.59**	**0.51**	**0.12**	**0.004**	**0.003**	**100.00**

This tidal range is comparable to the ±4.5 cm found by Papadopoulos (2009) for the station in the bay of Souda by obtaining the diurnal and semi-diurnal tidal components through yearly recordings.

Larger water level changes were also captured in the AWAC recordings, which include the longer fortnightly and monthly tidal constituents (excited mainly by fluctuations caused by meteorological phenomena such as wind stresses and atmospheric pressure, Tsimplis, 1994; Papadopoulos, 2009) as well as storm surge and the seasonal cycle in the study area. The total water level range (including tidal fluctuations and storm surge) in all AWAC deployment recordings was found to lie within ±24 cm.

3.3. Resonant frequencies

During the study, it was visually observed that overtopping along the docks of the western basin occurred when significant wave heights offshore exceeded 2 m. However, instrumentation was not deployed inside the harbour for all these events. The following recorded surface elevation time series inside the harbour, belonging to storm events between February 2015 and February 2019, were chosen for spectral analysis to identify the resonant periods at each deployment location:

- Storm 1: 10/02/15-12/02/15, 43 time series, $max(H_{1/3}) = 5.8$ m, location A.
- Storm 2: 08/04/15-11/04/15, 49 time series, $max(H_{1/3}) = 3.9$ m, locations A, D.
- Storm 3: 31/12/15-01/01/16, 21 time series, $max(H_{1/3}) = 2.4$ m, locations A, B, D.
- Storm 4: 05/02/16-06/02/16, 20 time series, $max(H_{1/3}) = 3.1$ m, locations A, B, D.
- Storm 5: 25/09/18-27/09/18, 41 time series, $max(H_{1/3}) = 3.0$ m, locations B, C, D.
- Storm 6: 13/02/19-15/02/19, 51 time series, $max(H_{1/3}) = 5.0$ m, locations B, C, D.

The main average offshore incident direction was north for all six storm events, while $max(H_{1/3})$ refers to the maximum offshore significant wave height of each event. The number of successive harbour surface elevation time series of 4096 s outlined above, corresponds to the time period during which the incident offshore significant wave heights exceeded 2 m.

Raw spectra derived through spectral analysis of the individual AWAC and pressure gauge time series of free surface elevation were averaged (at each frequency bin) over the duration of each storm event

(offshore $H_{1/3} > 2$ m) to obtain the storm-averaged spectra shown in Fig. 3. In order to examine the spectral energy distribution in the low frequency range and identify the harbour resonant frequencies at each location, the raw spectra from all selected storm events derived from time series recorded at each pressure gauge deployment location inside the harbour were averaged to obtain the storm-averaged spectra shown in Fig. 4; the frequency step of the pressure gauge storm-averaged spectra is $\Delta f = 2.44 \times 10^{-4}$ Hz (1/4096 s), which is sufficient to resolve the resonant frequencies of each location. The degrees of freedom of the storm-averaged spectra (displayed in Fig. 3 and the caption of Fig. 4) according to the χ^2 distribution (Goda, 2010) varies depending on the number of available time series at each location.

Due to the short duration of the AWAC recordings (20 min/h), the resulting spectral frequency resolution of the offshore storm-averaged spectra shown in Fig. 3 does not provide a detailed picture of the spectral energy distribution in the IG range. Further, since the offshore spectra are narrow banded and low frequencies are fetch-limited ($1/f <\sim 14$ s), sloshing inside the harbour must be driven by the release of free long waves from non-linear interaction of the storm waves offshore, and not by swell as was the case in other case studies (e.g. Okihiro et al., 1993; Okihiro and Guza, 1996).

In the sea-swell energy range, the highest spectral energy peaks at location A match the highest energy range of the offshore spectra, indicative of the intense penetration of the offshore storm waves and lack of protection of the main harbour entrance — field measurements at location A have registered significant wave heights of up to 1.6 m and maximum wave heights more than 2 m during severe storm events.

Location A experiences very little wave energy at around 8 s (0.12 Hz), while distinctive peaks appear at neighbouring 9 s (0.11 Hz) and 7 s (0.14 Hz). More specifically, during Storm 2, the 9 s energy peak concentrates double the amount of energy compared to the 7 s peak, likely as a result of the offshore spectrum featuring wave energy at periods above 9 s. In the less energetic Storm 4, the spectral energy at 7 s remains the same as for Storm 2, while the energy at 9 s drops significantly and becomes almost equal to the spectral energy at the 7 s peak.

At location B, the sea-swell spectral energy is more widespread and the spectral peaks are not as distinctive as in location A. By contrast, the storm-averaged spectrum for location C features pronounced energy peaks at 6 and 8 s during Storm 5. During more energetic Storm 6, the same energy peaks appear at location C, noticeably at lower energy values, but a new energy peak appears at $\sim$ 11 s (0.88 Hz) following the increased amount of offshore energy present at the same frequency range.

Location D is the most sheltered in the harbour, and it shows negligible amounts of energy in the sea-swell frequency range, with almost all of the energy concentrated in the IG range. The IG energy ($f < 0.04$ Hz) at location A, on average, is about 5% of the total during the storm events studied. At locations B and C, sea-swell (SS) energy overshadows IG, since both sites are in the more energetic western basin, In these two locations, IG energy rises to $\sim$ 20% of the total. At the most protected location D, the IG frequency range of the spectrum includes 88% of the total energy.

Fig. 4 shows the storm-averaged spectra for all storm events, for each of the four instrument deployment locations inside the harbour, focusing in the IG frequency range. Several distinct spectral energy peaks at narrow frequency bands are visible, with most being common between different deployment locations inside the harbour basins. These distinct peaks indicate wave amplification inside the basins at specific frequencies corresponding to the natural oscillation frequencies of the harbour.

Starting from the highest peak frequencies, the spectrum for location A peaks at 55.3 s period, for location B at 54.6 s and for location C at 56.1 s. Each of the peaks possibly corresponds to a different higher mode. No spectral energy peak appears at the 54.6–56.1 s frequency range for location D, presumably because these higher resonant modes only affect the western harbour basin. Instead, location D features a peak at period 60.2 s, at which period the spectra for locations A and B appear as nodal points, thus corresponding to a resonant mode affecting only the eastern basin.

The next frequency band featuring a distinct peak corresponds to periods ranging between 73.1–75.9 s. This peak features in the spectra of locations A, B and D. The next energy peaks are located at 89 and 95 s. The flatness of the energy spectra for locations A, C an D in the frequency range 89–95 s, and the fact that the spectrum for location B only features a distinct peak at 95 s, they can be interpreted as two resonant frequencies, one at 89 s, affecting locations A, C and D, and another at 95 s affecting all deployment locations. The next energy peak is at 132 s, which is prominent in the spectrum of location D, and to some extent at location C. Location B is unaffected, while the spectrum of location A exhibits a faint peak.

The most prominent energy peak is at 240 s, and is common for the storm-averaged spectra of all deployment locations inside the harbour. The following peaks appear at periods of 585 and 512 s for locations A–B and C–D, respectively. However, since the frequency difference corresponds to a single frequency step in the energy spectrum, it is possible that both frequency peaks correspond to the same frequency band. It will be shown in the next section that these two spectral peaks at period bands of 512–585 and 240 s correspond to the first two resonant frequencies of the harbour.

Last, there is a distinct peak at a period of 1365 s, which is common at all four locations. This very low frequency band is beyond the possible range of the harbour's natural oscillation periods. Also, due to the relatively coarse resolution of the storm-averaged spectra for all storm events derived from 4096 s time series at this low-frequency range, the peak at 1365 s actually corresponds to a wide frequency band (1170 s - 1638 s).

In order to obtain a more detailed picture of the spectral energy distribution at this low-frequency range, we did a separate spectral analysis using continuous free surface elevation data collected at location D during storm event 2. The continuous dataset with 1 Hz sampling frequency was divided into eleven time series of 24,576 s, resulting in a spectrum of resolution $\Delta f = 4.069 \times 10^{-5}$ Hz and 22 degrees of freedom. The higher-resolution averaged spectrum shown in Fig. 5 exhibits several peaks at discrete frequency bands beyond the 534 s period. These frequency bands likely correspond to the natural oscillation periods of a larger system, such as the entire bay of Chania.

4. Numerical modelling

We study the excitation of the Venetian harbour numerically using the Boussinesq-type COULWAVE model. COULWAVE in its present form solves a suite of governing equations at different approximations and numerical schemes (Lynett et al., 2008). In this study, we employ the fully non-linear, weakly rotational and weakly-dispersive BT equations, implemented through a finite-volume numerical scheme (Kim et al., 2009). Wave energy is dissipated through wave breaking, using a modified version of the Kennedy et al. (2000) model described in Løvholt et al. (2013), and a Mannings bottom-friction term.

Shallow-water wave equations models are generally not used in harbour resonance studies (Synolakis and Kânoğlu, 2015), but are used to study runup and wave amplification of tsunamis. BT models are computationally expensive compared to linear mild-slope models (e.g. CGWAVE, PHAROS, MIKE 21 EMS, etc.) typically employed for harbour resonance studies (e.g. Morison and Imberger, 1992; Okihiro et al., 1993; Bellotti, 2007; Modesto et al., 2020). However, BT models offer multiple advantages in return: (i) hydrodynamics are more accurately resolved from deep to shallow water, including energy dissipation due to wave breaking in the nearshore, (ii) wave runup can be simulated through moving boundary algorithms, therefore no empirical reflection coefficients need to be defined along the coastline, and (iii)

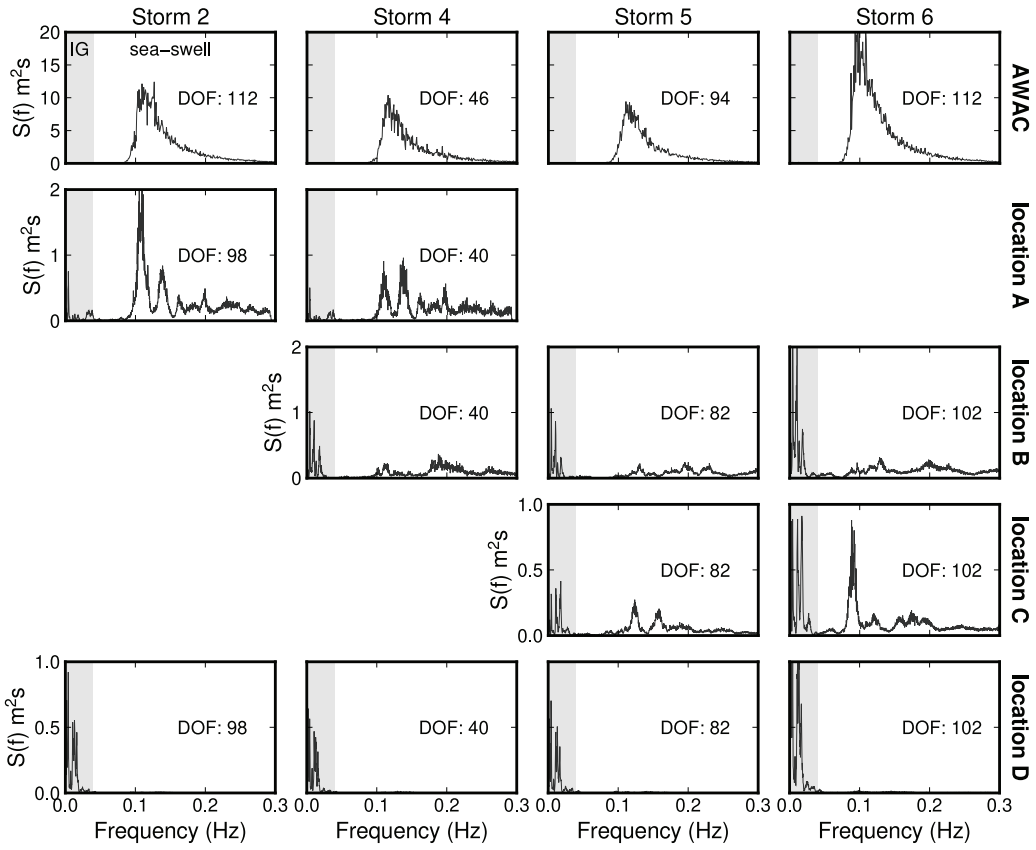

Fig. 3. Storm-averaged spectra for four selected storm events at the offshore deployment location (AWAC) and the four sensors deployed inside the harbour. Ordinate scales differ across location graphs. IG frequency range (grey shade) corresponds to $f < 0.04$ Hz. Displayed DOF values correspond to the degrees of freedom of each spectrum.

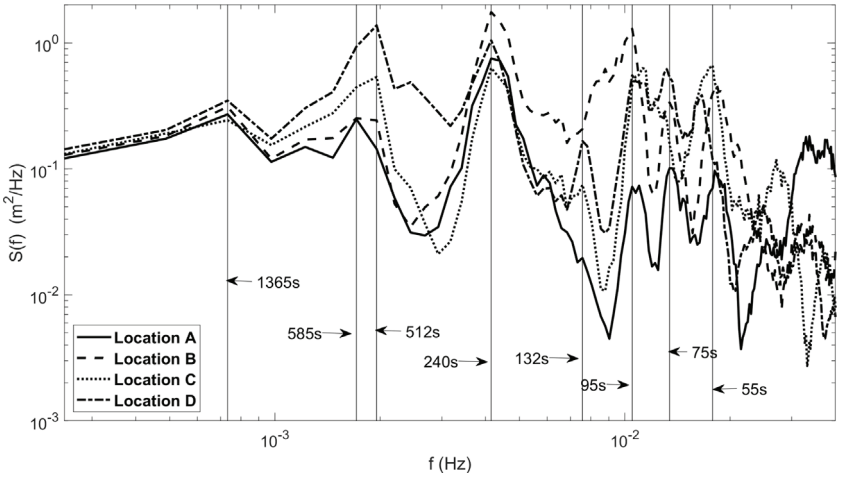

Fig. 4. Storm-averaged spectra at the four deployment locations inside the harbour using available time-series of 4096 s from all storm events with $H_{1/3} > 2$ m at each deployment location. The degrees of freedom of each spectrum are: 266, 266, 184 and 364 for locations A, B, C and D, respectively.

non-linear wave–wave interactions that generate IG energy (Longuet-Higgins and Stewart, 1964) are simulated, and thus realistic spectral boundary conditions can be imposed to predict meaningful harbour amplitudes and amplifications. The adequacy and benefits of BT models for harbour resonance studies have been demonstrated by Nwogu (2001). Douyere (2003) has specifically applied COULWAVE to study wave amplification due to resonance in Hawaiian harbours.

Our simulations were run on a 749 x 510, 2 m cell-sized numerical grid, which has adequate resolution to resolve the harbour features of hydraulic importance, such as the culvert in the eastern harbour basin (label 2, Fig. 1a). Bathymetric data were collected using the single beam echo sounder Sonar Mite (Ohmex Instruments), while topographic and shallow water relief data was collected using an RTK GPS system (Hiper Pro, Topcon). Bathymetric and topographic data were merged to create the seamless grid referenced at MWL shown in Fig. 1a.

We defined the offshore boundary conditions through a directional JONSWAP spectrum (e.g. Goda, 1988), representing an idealized northern storm with parameters $H_{m0} = 3.5$ m, $T_p = 8.5$ s, and $\gamma = 3.3$. The frequency step used in the input spectrum is $df = 0.002$ Hz. The spectral energy was curtailed at 5% of the peak energy (defined at $f = 1/T_p$) on both the high-frequency and low-frequency limit of the directional spectrum, corresponding to $f_{max} = 0.205$ and $f_{min} =$

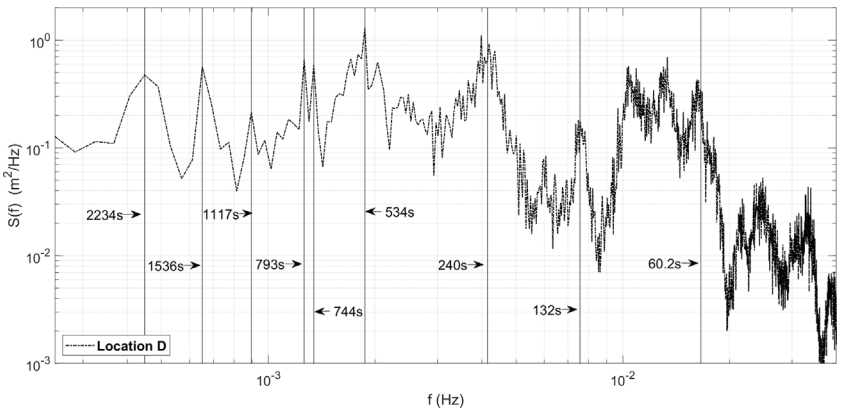

Fig. 5. Energy density spectrum at location D for storm event 2, using 24,576 s time series and 22 degrees of freedom, and the periods corresponding to selected spectral peaks.

0.085 Hz, respectively (Fig. 7a). The energy of the curtailed spectrum was not rescaled resulting in a reduced spectral significant wave height H_{m0} = 3.4 m. The JONSWAP input parameters are based on offshore conditions recorded during the initial stages of Storm 6, when for four consecutive hours significant wave heights ranged between 3.2–3.5 m and peak periods between 8.2–9.0 s; the COULWAVE input JONSWAP spectrum and the corresponding (recorded) target offshore spectrum are shown in Fig. 6a.

The directional spectrum $G(\theta|f)$ was set after Mitsuyasu et al. (1975) to

$$G(\theta|f) = G_0 \cos^{2s_m}\left(\frac{\theta}{2}\right), \theta \in [-10, 10], \quad (1)$$

where s_m is the directional spreading factor and θ is the azimuth measured with respect to the principal wave direction (Goda, 2010). The directional spreading factor was set at $s_m = 80$ based on the decay of the AWAC-derived directional energy distribution within ±10 deg around the principal wave direction (north in this case), where the directional spectrum was cut off.

Open boundary conditions were used for the northern, eastern and western boundaries of the computational domain, where reflected waves were absorbed through sponge layers as recommended by Kirby et al. (1998). No empirical reflection coefficients were used along the coastline. The input relief grid of 2 m cell size features steep slopes at the harbour's vertical walls (Fig. 1b-e) which induces the reflections in the simulation through the model's moving boundary algorithm (Lynett et al., 2002). A constant depth region was created below 20 m depth and the input directional spectrum was forced through an internal source generator combined with the sponge layer on the northern boundary.

The model run simulated 200 min of physical time, with the first 20 min disregarded as "model warm up" to allow the simulation to reach a quasi steady state. Surface elevation information was stored on a 10m-spaced array and the spectral energy density in each node was obtained through FFT analysis (with frequency step $\Delta f \sim 10^{-4}$ Hz). The resulting simulated H_{m0} distribution inside and offshore the harbour basin is illustrated in Fig. 6b. The insufficient offshore protection of the harbour is evident from the high H_{m0} values found in the western basin, particularly in the area between the harbour entrance and the NW-facing dock of the western basin, where H_{m0} values range between 1–1.5 m. Wave statistical parameters controlling wave overtopping derived through the pressure gauge recordings in harbour deployment locations B, C and D that correspond to the offshore wave conditions shown in Fig. 6a are compared with the COULWAVE predictions in Table 2. The numerical results are generally in good agreement with the field measurements.

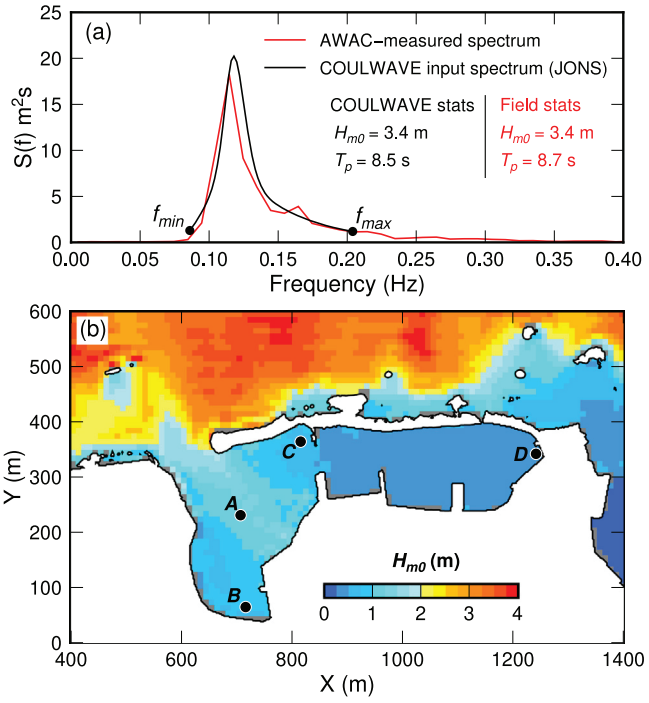

Fig. 6. (a) Comparison between the JONSWAP input spectrum to the COULWAVE simulation (black line) and the representative measured offshore conditions (red line). (b) COULWAVE-simulated H_{m0} distribution inside the harbour basin and offshore. (For interpretation of the references to colour in this figure legend, the reader is referred to the web version of this article.)

Table 2
Comparison of spectral wave parameters derived from pressure gauge field measurements in deployment locations B, C and D, and COULWAVE numerical results for the storm event shown in Fig. 6: H_{m0} is the significant wave height over the whole frequency range, $H_{m0,IG}$ is the significant wave height in the IG frequency range (0–0.04 Hz), and $T_{m-1,0}$ is the spectral period controlling wave overtopping. The parameters were derived using field and numerical free surface elevation time series of 4096 s; the field-extracted parameters were derived using the closest (in time) pressure gauge time series to the AWAC measurements.

	Location B		Location C		Location D	
	Field	Coul	Field	Coul	Field	Coul
H_{m0} (m)	0.83	0.86	0.67	0.67	0.40	0.41
$H_{m0,IG}$ (m)	0.39	0.44	0.30	0.30	0.37	0.37
$T_{m-1,0}$ (s)	43.0	36.3	42.8	48.5	233	252

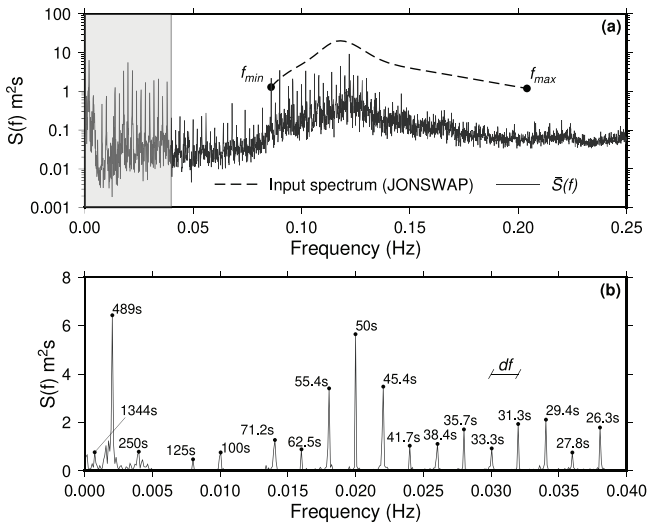

Fig. 7. (a) Space-averaged spectrum computed from the COULWAVE free surface elevation time series inside the harbour basin compared to the JONSWAP spectrum forcing the offshore boundary conditions. Shaded area denotes the IG frequency range of the space-averaged spectrum blown out in (b).

4.1. Harbour basin resonant frequencies and modes

The resonant frequencies of the basin were identified using the space-averaged spectrum, as defined in (Douyere, 2003),

$$\bar{S}(f) = \frac{1}{N}\sum_{i=1}^{N} S_i(f), \tag{2}$$

where $S_i(f)$ is the spectral energy of node i in the harbour basin, and N is the number of cells inside the basin. The space-averaged spectrum was utilised to identify the frequency bins of wave energy concentration, and in combination with the inspection of the individual spectra, it provides a snapshot of the harbour excitation (Douyere, 2003).

Fig. 7a compares the resulting space-averaged spectrum inside the harbour basin to the input JONSWAP spectrum. Due to offshore wave breaking and sheltering of the harbour basin, the space-averaged spectrum has considerably less energy across the sea-swell frequency range. The numerical model generates energy in higher and lower frequencies than f_{max} and f_{min}, respectively, as a result of non-linear wave–wave interaction in the surf zone, part of which is being released in the form of free waves (Longuet-Higgins and Stewart, 1962, 1964).

The dominant frequency peaks in the IG-range which result from the spatial averaging of the (harbour basin) numerical time series are shown in Fig. 7b. A considerable number of resonant periods are close or identical to the ones identified from the field measurements (in parentheses): 125 s (132 s), 100 s (95 s), 71.2 s (73 s–76 s), 62.5 s (60.2 s), 55.4 s (55.3 s–56.1 s), 38.4 s (36.9 s), 31.3 s (30 s) and 27.8 s (27 s). The simulated resonant periods of 489 s and 250 s are not captured at any of the sensor deployment locations. Instead, the closest resonant periods in the measurements correspond to 512 s and 240 s, respectively.

Fig. 7b reveals how the wave energy is contained within regular frequency bins with step df. The model is thus able to resolve resonant frequencies within $\pm df/2$. On the other hand, the detection of resonant frequencies identified through the field measurements is limited by the FFT frequency step, which is a function of the length of the free surface elevation time series (T_{FSE}), i.e. $\Delta f = 1/T_{FSE}$. Therefore, resonant periods T_n identified through the numerical model (peaks in Fig. 7b) lie within a range of $T_n \pm df/2$, and resonant periods identified through the field measurements (peaks in Fig. 4) lie within a range of $T_n \pm \Delta f/2$. Taking the dependence on df and Δf into account, a more accurate comparison between resonant frequencies predicted by the model and the ones measured through field measurements is presented in Table 3.

A spatial overview of the harbour excitation model predictions is given in Fig. 8 for the first eight resonant frequencies. The modes of oscillation show the distribution of spectral energy corresponding to each resonant frequency. The mode of the resonant period of 489 s (512 s) exhibits a node at the harbour entrance and an antinode on the eastern-most point and corresponds to the zeroth mode of a long and narrow open-ended basin, known as the *Helmholtz* or *gravest mode* (Rabinovich, 2009); again, the corresponding field measurement is stated in the parenthesis. The mode of the resonant period of 250 s (240 s) features two antinodes at the two ends of the harbour basin and a node midway, and corresponds to the *fundamental mode* of a long and narrow closed basin (Rabinovich, 2009). The distribution of spectral energy across the basin for the Helmholtz and fundamental modes is in agreement with the distribution of measured spectral energy at ~ 512 and 240 s (Fig. 4) relative to the deployment location of the four pressure gauges.

The resonant periods of 125 s (132 s), 100 s (95 s), 71.2 s (73 s–76 s) correspond to the second, third and fourth modes of a long and narrow closed basin, featuring two, three and four nodes, respectively. The modes for the resonant periods of 62.5 s (60 s) and 55.4 s (55 s) involve two-dimensional basin effects with harbour oscillations also occurring along the width of the basin. Last, the mode for the energetic resonant period of 50 s only involves the western harbour basin. It is the *rocking* mode of the western basin and which corresponds to sloshing occurring between the harbour entrance and the dock directly impacted by the incoming storm waves.

5. Overtopping discharge due to harbour resonance

Here, we attempt to quantify the influence of harbour resonance on wave overtopping along the docks, a process that is not well understood, and to our knowledge has not been examined before. This is particularly important in view of the already-happening sea level rise. Wave overtopping discharges were evaluated at 20 locations along the perimeter of the western harbour basin (Fig. 9). During storm events, it has been observed that the magnitude and type of wave overtopping vary along the docks. Locations 1–15 suffer from green-water type overtopping while locations 16–20 are impacted, depending on the storm intensity, by heavy loads with up-rushing water jets overtopping them. At the western side (locations 1–8) overtopping is caused from diffracted and partially refracted waves approaching the docks in wide angles, with reflected waves contributing periodically to increased overtopping discharges. Along the southern locations (9–11), incident waves are approaching the docks in normal directions coming from the harbour entrance, but here wave reflections have a larger contribution to overtopping than incident waves. Southeast dock locations (12–15) are overtopped mainly by waves strongly reflected at that part of the basin, forming standing waves. Locations 16–20 directly face the unprotected entrance; waves approach the docks from the entrance on an oblique angle (~ 20° angle anticlockwise to the normal wave incident direction, see Fig. 9), shoaling up and eventually impacting the docks in impulsive conditions.

5.1. Wave overtopping formulas

We employ the empirical equations of EurOtop (2018) to estimate the mean overtopping rates using the mean value approach (without including a safety factor for structural design). The EurOtop equations provide overtopping discharge predictions for structures facing the open sea. While this is clearly not the case for a harbour basin, they are the only established choice for such estimates.

A range of empirical equations are available in the EurOtop manual depending on the characteristics of the incident waves (wave height, period and direction), the type of structure considered (breakwater,

Table 3
Detection upper and lower limits for the basin resonant periods (in seconds) through the numerical simulation, and field measurements at instrument deployment locations $A - D$.

	Field measurements								COULWAVE	
	A		B		C		D			
	$T_{n,min}$	$T_{n,max}$	$T_{n,min}$	$T_{n,max}$	$T_{n,min}$	$T_{n,max}$	$T_{n,min}$	$T_{n,max}$	$T_{n,min}$	$T_{n,max}$
Helmholtz mode	546	630	546	630	481.9	546.1	481.9	546.1	328.3	956.1
Fundamental mode	234.1	248.3	234.1	248.3	234.1	248.3	234.1	248.3	200.0	333.5
2nd mode	–	–	–	–	129.9	134.2	129.9	134.2	111.1	142.9
3rd mode	93.9	96.1	93.9	96.1	88	90	93.9	96.1	90.6	110.6
4th mode	72.5	73.8	73.8	75.2	76.6	78	75.2	76.6	66.5	76.7
5th mode	–	–	–	–	–	–	59.8	60.6	58.8	66.7
6th mode	54.9	55.7	54.2	55	55.7	56.5	–	–	52.5	58.7
7th mode	–	–	49.7	50.3	49.7	50.3	–	–	47.6	52.5

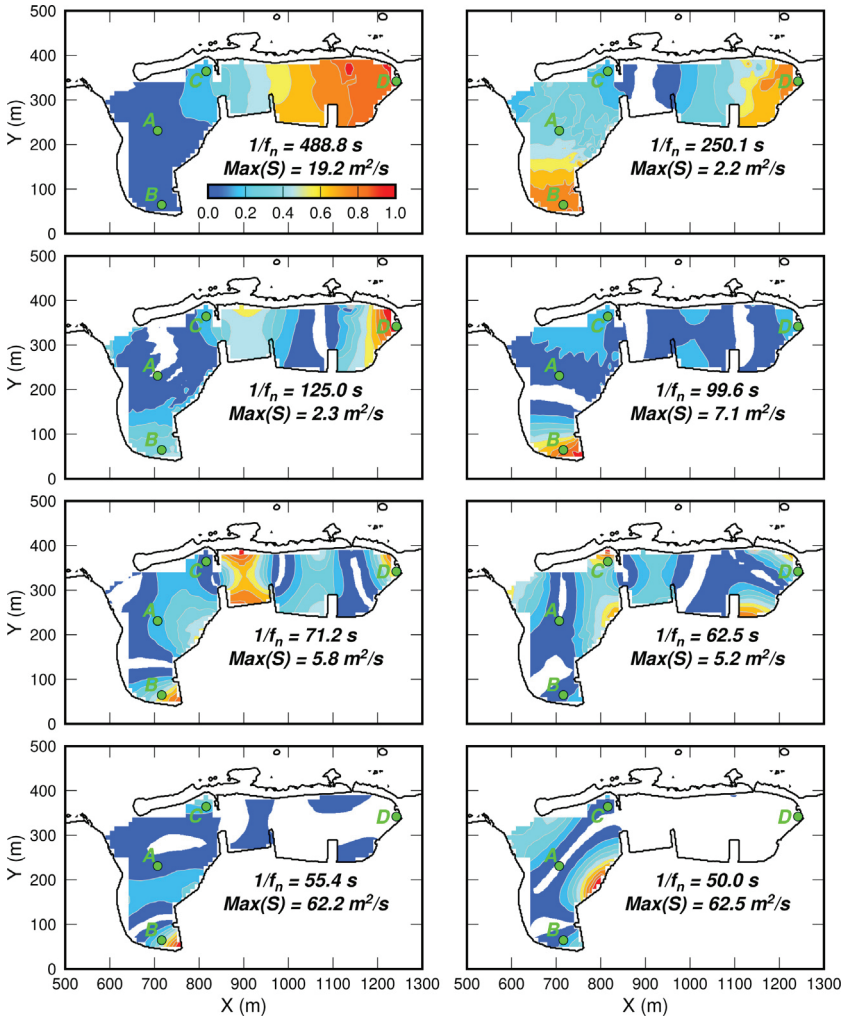

Fig. 8. Modes corresponding to the first eight resonant frequencies identified for the harbour basin through the numerical simulation. The colourmap has been normalised by the maximum spectral energy for each resonant frequency (*Max(S)*) registered across the harbour basin nodes. Spectral energy values two order of magnitudes less than *Max(S)* appear as white. Instrument deployment locations $A - D$ are shown with the green circles. (For interpretation of the references to colour in this figure legend, the reader is referred to the web version of this article.)

dyke, vertical wall, etc.), and finally the influence of the foreshore with length equal to $L_{m-1,0}$ (the wavelength corresponding to $T_{m-1,0}$) evaluated at the toe of the structure. The EurOtop equations for vertical and steep walls were used for the harbour docks. We then inferred the influence of the foreshore to account for the effect of obliquity of the incident waves, which may lead to impulsive or non-impulsive conditions.

We used the following steps to determine the appropriate overtopping discharge equation:

- **Step 1**: The influence of foreshore was taken into consideration without the presence of a significant mound, and with the toe of the structure submerged ($h > 0$).
- **Step 2**: We determined if impulsive or non-impulsive conditions occur for shore-normal wave-attack using

$$\begin{cases} \dfrac{h^2}{H_{m0} L_{m-1,0}} > 0.23 & \text{(non-impulsive conditions)}, \\ \dfrac{h^2}{H_{m0} L_{m-1,0}} \leq 0.23 & \text{(impulsive conditions)}, \end{cases} \tag{3}$$

where h is the water depth at the toe of the structure and H_{m0} is the spectral significant wave height. Then, we determined the overtopping rates for shore-normal incidence.

For non-impulsive conditions, we used the overtopping discharge equation

$$\frac{q}{\sqrt{gH_{m0}^3}} = 0.05\exp\left(-2.78\frac{R_c}{H_{m0}}\right), \tag{4}$$

where R_c is the crest freeboard (m) and q is the overtopping rate (m^3/s, per m along the dock).

For impulsive conditions, the corresponding equation is

$$\frac{q}{\sqrt{gH_{m0}^3}} = 0.011\sqrt{\frac{H_{m0}}{hs_{m-1,0}}}\exp\left(-2.2\frac{R_c}{H_{m0}}\right), \quad \text{for } 0 < \frac{R_c}{H_{m0}} < 1.35, \tag{5}$$

or

$$\frac{q}{\sqrt{gH_{m0}^3}} = 0.0014\sqrt{\frac{H_{m0}}{hs_{m-1,0}}}\left(\frac{R_c}{H_{m0}}\right)^{-3}, \quad \text{for } \frac{R_c}{H_{m0}} \geq 1.35, \tag{6}$$

where $s_{m-1,0}$ is the wave steepness defined as $s_{m-1,0} = H_{m0}/L_{m-1,0}$.

- **Step 3**: Under the influence of oblique waves and non-impulsive conditions, q is estimated through

$$\frac{q_\beta}{\sqrt{gH_{m0}^3}} = 0.05\exp\left(-\frac{2.78}{\gamma_\beta}\frac{R_c}{H_{m0}}\right), \tag{7}$$

where γ_β is a reduction factor for angle of attack and is given by

$$\begin{cases} \gamma_\beta = 1 - 0.0033|\beta| & (\text{for } 0 \leq \beta \leq 80°), \\ \gamma_\beta = 0.736 & (\text{for } |\beta| > 80°), \end{cases} \tag{8}$$

and β is the incident angle relative to the vertical of the dock's orientation (EurOtop, 2018).

- **Step 4**: In case of oblique incident waves and impulsive conditions, equations of Step 3 should be used when waves approach with $\beta \geq 60°$. For incident angles less than 60°, wave overtopping estimates are based on results for $\beta = 15°$ and $\beta = 30°$. The influence of oblique wave attack is characterised by an obliquity factor $k_\beta = q_\beta/q_{\beta=0°}$, where $q_{\beta=0°}$ is the overtopping rate for shore-normal wave attack (EurOtop, 2018). Values of k_β for 15° and 30° are given by

$$k_{\beta=15°} = \max\begin{cases} 0.375\left(\frac{h^2}{H_{m0}L_{m-1,0}}\frac{R_c}{H_{m0}}\right)^{-0.46} \\ \exp\left(-0.267\frac{R_c}{H_{m0}}\right) \end{cases} \quad \text{for } \beta = 15°, \text{ with max } k_\beta = 1, \tag{9}$$

$$k_{\beta=30°} = \max\begin{cases} 0.454\left(\frac{h^2}{H_{m0}L_{m-1,0}}\frac{R_c}{H_{m0}}\right)^{-0.96} \\ \exp\left(-0.495\frac{R_c}{H_{m0}}\right) \end{cases} \quad \text{for } \beta = 30°, \text{ with max } k_\beta = 1. \tag{10}$$

Wave overtopping discharge predictions for any given incident angle were obtained through linear interpolation. Eqs. (9) and (10) are applicable in the range $1.35 \leq R_c/H_{m0} \leq 4$. The relative freeboard was less than 1.35 only in location 5, but since $\beta = 68°$, it was treated as under non-impulsive conditions and the overtopping prediction equations of Step 3 were used.

Eqs. (4), (5) and (6) correspond to equations (7.5), (7.7) and (7.8) of the EurOtop (2018) manual, while Eqs (7), (9) and (10) correspond to equations (7.16), (7.18) and (7.19), respectively. The use of Eq. (8) to compute the reduction factor for oblique attack in coastal dikes or embankment seawalls under non-impulsive conditions, which corresponds to (5.29) in the EurOtop manual, is also recommended for vertical walls (EurOtop, 2018).

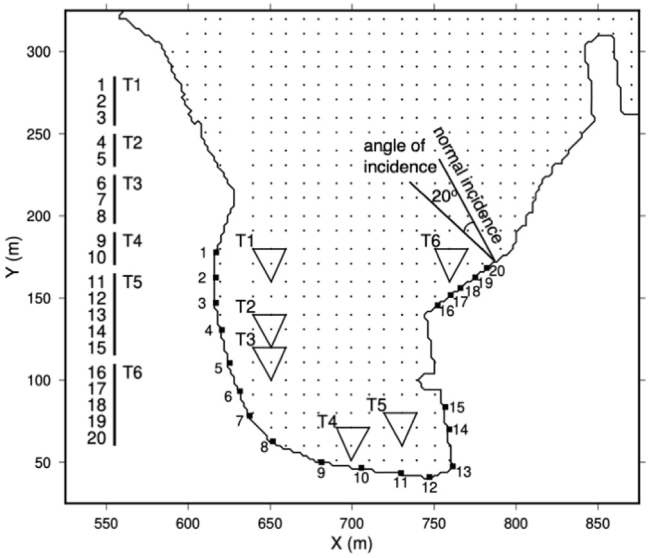

Fig. 9. Wave overtopping prediction locations along the western basin perimeter (squares). Black dots denote the nodes (numerical gauges) where numerical free surface elevation time series were recorded. Triangles denote the numerical gauge triads used to generate directional spectra and extract the input wave parameters for the overtopping predictions. The displayed angle of incidence (measured from the normal wave incident direction) corresponds to locations 16–20. The gauge triad correspondence to overtopping evaluation locations is outlined on the left.

5.2. Input parameters for EurOtop formulas

The geometrical input parameters for the above wave overtopping prediction formulas, such as the water depth at the toe of the structure and freeboard, were defined through a detailed topographic survey. The incident wave parameters were derived from the numerical time series stored at 10m-spaced nodes (gauges) inside the harbour basin. Triads of numerical gauges, tied to overtopping prediction locations along the dock (Fig. 9), were selected to produce wave directional spectra using the Extended Maximum Entropy Method (EMEM, Hashimoto et al., 1997). The directional spectra were then used to determine the mean incident wave direction ϕ. In turn, a 1D energy density spectrum was extracted by integrating the directional spectrum along the directions vector within the range $\phi \pm 22.5°$. From this point on, two distinct methodologies are applied to determine the wave overtopping input parameters (illustrated in Fig. 10):

- **Approach A**: The first approach attempts to examine and quantify the influence of harbour resonance on wave overtopping discharges along the harbour dock. The incident significant wave height H_{m0} and spectral period $T_{m-1,0}$ used with the EurOtop formulae were computed from the triad 1D power spectra, using only the wave energy contained in the high-frequency range (HF, $f >$ 0.04 Hz). These incident wave parameters represent the harbour basin wave climate excluding sloshing. The influence of harbour resonance was quantified through numerical time series of free surface elevation recorded nearest to each evaluation location along the dock. IG-motions η_{IG} contained in the time series were isolated through spectral analysis. η_{IG} was subtracted from the freeboard at still water level ($R_{c,SWL}$), producing a freeboard time series $R_{c,IG} = R_{c,SWL} - \eta_{IG}$. Wave overtopping using the EurOtop formulae was computed first for $R_{c,SWL}$, producing $q_{HF,SWL}$, and

then for the IG-adjusted freeboard values $R_{c,IG}$, producing time series $q_{HF,ADJ}$. The difference between the mean value of time series $q_{HF,ADJ}$ ($\bar{q}_{HF,ADJ}$) and $q_{HF,SWL}$ quantifies the influence of harbour resonance on wave overtopping along the docks.

- **Approach B**: The second approach corresponds to the conventional application of EurOtop formulae, which is used to provide context to the overtopping discharges predicted using Approach A. The incident significant wave height H_{m0} and spectral period $T_{m-1,0}$ were computed from the triad 1D power spectra, using the entire frequency range (IG and HF). EurOtop formulae were then applied to each evaluation location using the freeboard corresponding to SWL, resulting in overtopping discharge prediction $q_{HF-IG,SWL}$.

As described in Section 5.1, mean overtopping rates were estimated for both normal and oblique incident wave conditions to compare results between the two conditions and also because estimation of overtopping rates of normal incident waves was a prerequisite for the estimations in oblique conditions. Most locations resulted in impulsive incident conditions. However, using Approach A, locations 19–20 resulted in non-impulsive conditions for both normal and oblique incidence due to high values of the ratio in Eq. (3). Also, for oblique incidence, using Approaches A and B, locations 4–5 and 14–15 result in non-impulsive conditions due to the wider angles of incidence ($\beta > 60°$). For non-impulsive conditions, the prediction Eqs. (4) and (7) used to compute the mean overtopping rate for normal and oblique incidence, respectively, do not include the effect of the spectral period.

5.3. Overtopping results

Estimates of $q_{HF,SWL}$ (overtopping rates using spectral inputs for $f > 0.04$ Hz and no freeboard adjustment) for normal incident conditions are higher in comparison to oblique ones, at every evaluation location (Fig. 11). Notably, the lowest overtopping rates were calculated at predictions locations 14 and 15 for oblique incidence, due to maximum glancing angles and non-impulsive conditions. Another interesting observation is that, for the triad T5 chosen, more reflected energy was observed in the numerical directional spectra than elsewhere. These observations are consistent with eyewitness accounts for the particular storm used in the numerical simulation. At the locations facing the entrance (16–20), although common wave parameters and incident angles were extracted from triad T6, overtopping rates decrease from location 16 to 20, mainly due to differences in the corresponding toe depths.

In normal incident conditions, overtopping rates vary differently than in oblique conditions, because of the absence of incident angles in the calculations. Rate prediction values for locations 9–15 are very close due to similarities in the freeboards and incident wave parameters. The largest differences are found for locations 4–6, which is mainly attributed to the relatively low freeboards (location 5 has the lowest freeboard at 0.42 m) and to a lesser extent to the incident wave parameters — the significant wave heights extracted from triads T1–T3 were not the largest. High oblique angles and non-impulsive conditions reduced the overtopping rate in locations 4–6 (as in locations 14–15) for oblique incidence, consistent with eyewitness observations for the wave conditions simulated. During larger storms ($H_{1/3} > 4.5$ m), locations 4–6 experience the highest overtopping rates due to green-water overtopping, consistent with what is predicted using the normal incident angles.

Following Approach A, the effect of harbour resonance is added into the equation by varying the freeboard using the IG time series at the toe of each prediction location. The resulting overtopping rate, $\bar{q}_{HF,ADJ}$, shown in Fig. 11, is higher than $q_{HF,SWL}$ at all locations. This outcome can be interpreted as the non-linear behaviour of the wave overtopping equations to changes in the freeboard, i.e. increasing and decreasing the freeboard does not result in proportional changes to the overtopping rate predictions as wave overtopping discharge is exponentially related to R_c/H_s. This non-linear behaviour is more pronounced for normal incidence at prediction locations 4–6, which exhibit the lowest freeboards. In these locations, small changes in the freeboard, in the form of long-period fluctuations, result in disproportionately larger overtopping rates compared to locations with higher freeboards.

When the amplitudes of natural oscillations temporally superimpose, the freeboard is significantly reduced, resulting in sporadic bursts of high overtopping volume that significantly affect the mean overtopping rate; this effect was more pronounced for normal incidence at prediction location 4. Thus, docks with smaller freeboards are the most affected from wave overtopping due to harbour resonance. Changes between $\bar{q}_{HF,ADJ}$ and $q_{HF,SWL}$ are less pronounced for oblique incidence, because points of low freeboard happen to exhibit less wave overtopping for the simulated storm conditions due to the angles of incidence ($\beta > 20°$).

Comparing overtopping rates $q_{HF-IG,SWL}$ derived using the conventional application of EurOtop formulae (Approach B) with overtopping rates $\bar{q}_{HF,ADJ}$ calculated using Approach A, the former are on average two times higher than the latter, both for normal and oblique incident conditions. Thus, in general, accounting for the IG wave energy directly through spectral parameters H_{m0} and $T_{m-1,0}$ yields higher overtopping rates compared to Approach A for this case study. In fact, the ratio $q_{HF,SWL}/q_{HF-IG,SWL}$ is on average 0.50 and 0.46 for normal and oblique incidence, respectively, while the corresponding values for the ratio $q_{HF,SWL}/\bar{q}_{HF,ADJ}$ are 0.79 and 0.74. However, Approach A yields higher overtopping rates at locations with very low freeboards; $\bar{q}_{HF,ADJ}$ is higher than $q_{HF-IG,SWL}$ at prediction locations 4–5 for oblique wave incidence and higher only for location 4 for normal wave incidence. Another observation is that for locations 19–20, there is a significant difference between the prediction rates of the two approaches. This is partially due to the non-impulsive conditions used in Approach A, that did not account for the effect of the spectral period in the calculation of the overtopping rate prediction.

Approach A produces time series of wave overtopping rate ($q_{HF,ADJ}$) that allows to examine its temporal characteristics. Here, we examine the temporal characteristics of time series $q_{HF,ADJ}$ produced for all prediction locations assuming normal wave incidence. This was achieved by computing the spectra of each time series using FFT. After inspection, similarities in the spectra between prediction locations allowed us to present the spectra in four groups, as shown in Fig. 12. As expected, the $q_{HF,ADJ}$ spectra for all groups exhibit prominent peaks at the resonant frequencies identified through numerical modelling in Section 4.

The locations included in group *a* (locations using triads T1 and T2) are positioned along the western dock, which according to Fig. 8 is not a major antinode for any of the first 8 modes shown. As a result, the overtopping rate is well distributed among different frequency bins. The largest wave overtopping rate contributor is the frequency bin around 31.3 s period, which is a higher resonant mode not shown in Fig. 8. The 45.5 and 55.3 s resonant periods are second closest, which feature a weak antinode along the central part of the western basin. However, weaker contributions from the Helmholtz, fundamental and the 3rd frequency resonant modes are also visible. Group *b* (locations using triads T3 and T4) has similar characteristics to group *a*, albeit the spectral peaks are of lower magnitude.

In general, locations in group *c* (locations using triad T5) exhibit lower overtopping rates compared to locations in groups *a* and *b*. However, it is sitting right at the antinode of many resonant modes, as shown in Fig. 8. The most energetic mode at this antinode corresponds to the resonant period of 55.3 s that only involves the western basin. Similar but smaller modal amplitudes resulting from the 50.0 and 45.5 s resonant periods can also be distinguished in the spectrum.

Group *d* (locations using triad T6) involves the prediction locations facing the entrance. This part of the western basin is mainly affected by the resonant periods around 50 s that create energetic antinodes

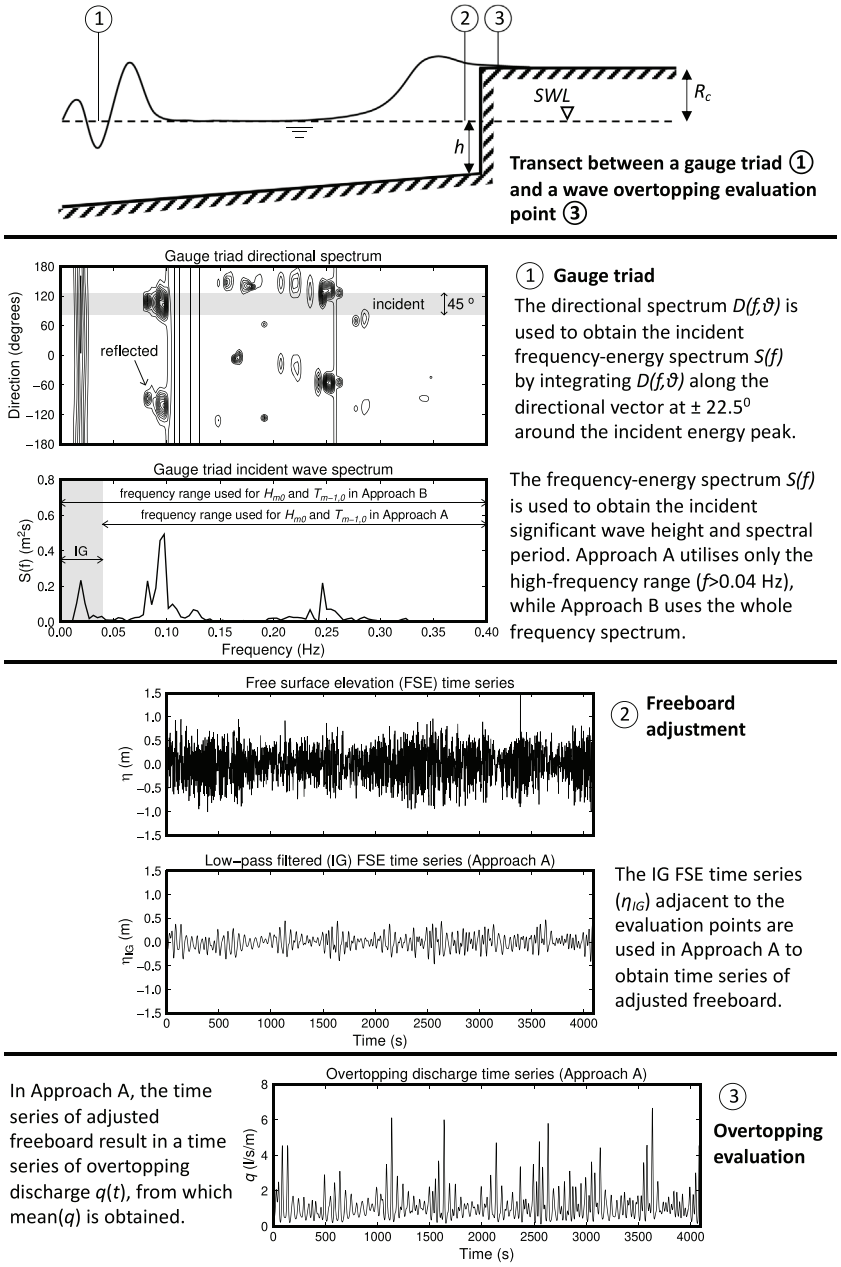

Fig. 10. Illustration of the proposed Approach A used to evaluate the contribution of harbour resonance on wave overtopping along the docks.

along the dock of group *d* (Fig. 8). As a result, overtopping rates feature prominent peaks around the resonant periods of 45.5, 50 and 55.3 s. There are added contributions from higher resonant modes at periods below 35 s.

6. Discussion and conclusions

This study investigated the resonant frequencies and modes of a small, irregularly shaped harbour with two basins. The wave climate offshore the Venetian Harbour of Chania was characterised through in situ measurements using an ADCP deployed at ∼ 23 m depth, for a nine year period. The data recording plan of 2 Hz sampling rate for 1200 s/h allowed us to obtain the offshore wave field (1200 s provide reliable statistical results), while also capturing its temporal development in detail through hourly intervals. However, the sampling duration of the individual time series was not sufficient to obtain the spectral resolution required to study the offshore energy distribution in the infragravity frequency range in detail. Thus, it was not attempted to correlate the infragravity energy distribution offshore and inside the harbour.

The resonant frequencies of the harbour basin identified through field measurements at four different deployment locations during several storm events, offer insight on the response of the basin to offshore forcing. The storm-averaged spectra for all storm events feature distinctive peaks and troughs at specific frequency bands (Fig. 4). The frequencies corresponding to each peak represent resonant frequencies at which spectral energy is amplified due to sloshing. The frequencies of the spectral energy peaks identified from the individual storm-averaged spectra corresponding to each of the four deployment locations generally agree well. However, small frequency deviations were found for some of the spectral peaks. For example, the frequency peak corresponding to the spectral peak of the fundamental mode (i.e. at T_n = 240 s) is common between the spectra of all four locations, but the frequency peak corresponding to the Helmholtz mode is not. This

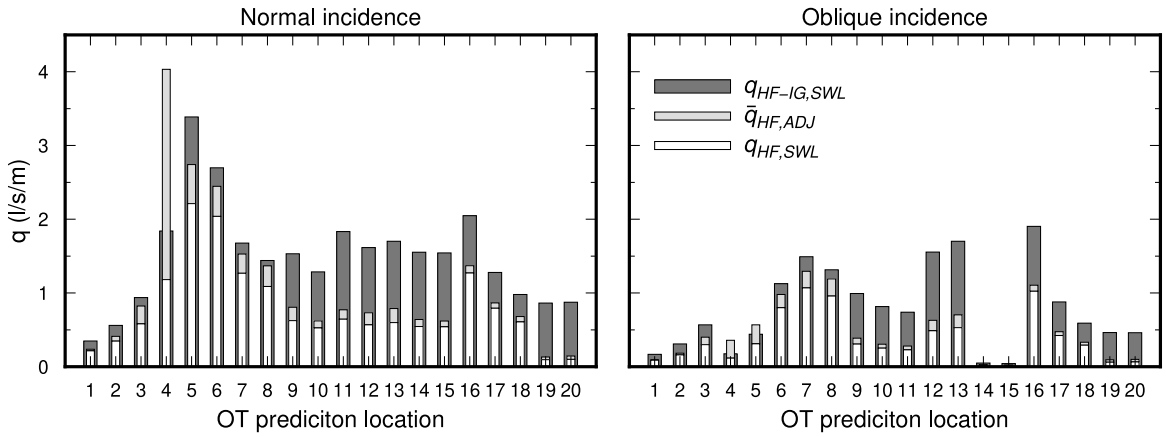

Fig. 11. Mean wave overtopping rate estimates at the locations shown in Fig. 9. $q_{HF-IG,SWL}$ and $q_{HF,SWL}$ correspond to the mean overtopping rates using the crest freeboard relative to SWL and wave incident characteristics from the full and the higher frequency range ($f > 0.04$ Hz), respectively, and $\bar{q}_{HF,ADJ}$ corresponds to the mean overtopping rate of time series $q_{HF,ADJ}$ computed using the higher frequency wave incident characteristics and freeboard $R_{c,IG}$ which is adjusted using IG free surface elevation time series at the toe of the structures.

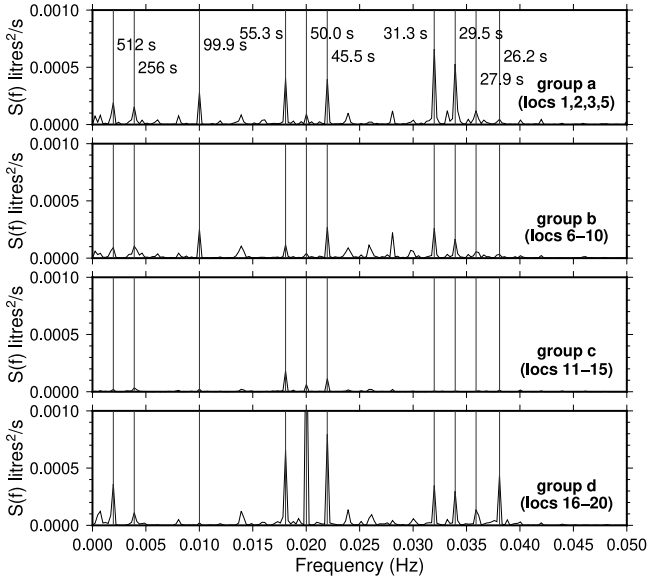

Fig. 12. Spectra of the time series of overtopping rate produced using Approach A for normal wave incidence. The spectra have been averaged in groups of similar spectral distributions (prediction locations referred here are shown in Fig. 9).

resonant frequency deviation can be attributed to the relatively coarser period resolution at the frequency range of the Helmholtz mode.

Numerical simulations using the Boussinesq-type model COULWAVE and a JONSWAP offshore spectrum provide a detailed picture of the wave climate inside the harbour basin; the input spectrum only contains energy in the sea-swell frequency range using a constant frequency step df and infragravity energy was generated through non-linear interactions of the input frequency components. The mean spectral energy inside the basin was derived by space-averaging the spectra of all numerical time-series collected inside the harbour basin. Spectral energy in the infragravity range is contained in peaks at discrete frequencies driven by harbour resonance. However, by forcing the offshore spectral energy using a constant frequency step df, the spectral peaks are also positioned at frequency steps that are multiples of df and not necessarily at the true resonant frequencies.

As a result, the basin was forced at frequencies closer to the actual resonant frequencies in the higher-frequency range compared to the lower-frequency range — the spectral leakage is particularly evident around the Helmholtz and fundamental resonant frequencies (Fig. 7b). This limitation does not allow us to directly compare the total energy contained in each resonant frequency. However, it is still evident that the Helmholtz mode is very energetic and also that the 50 s resonant period has comparable mean energy to the Helmholtz mode across the harbour, even though it only involves the western basin (Fig. 8).

Despite this, the resonant frequencies identified through numerical modelling generally compare well with the field data. No attempt was made to compare the relative energy of each resonant frequency predicted by the model to the storm-averaged spectra since the spectra produced through the field data used different storm events for each location (of varying intensity and duration). The spatial distribution of spectral energy across the basin provides an overview of the modes corresponding to each resonant frequency, through which the Helmholtz, fundamental and higher modes were identified (Fig. 8). The distribution of energy of each mode is consistent with the spectral energy of the resonant peaks in the storm-averaged spectra relative to the corresponding deployment locations.

The numerical time series were used in combination with EurOtop formulae to obtain wave overtopping rates at evaluation points along the western basin docks and investigate the influence of resonance on wave overtopping. Two different approaches were used for that purpose: Approach B producing $q_{HF-IG,SWL}$ involved the conventional application of EurOtop wave overtopping formulae, and novel Approach A producing $q_{HF,SWL}$ and $\bar{q}_{HF,ADJ}$ that was used to infer the contribution of harbour resonance to wave overtopping. Comparing $q_{HF,SWL}$ with $q_{HF-IG,SWL}$ allowed us to examine the importance of IG energy in wave overtopping along the harbour docks. Excluding evaluation points 19 & 20, the ratio $q_{HF,SWL}/q_{HF-IG,SWL}$ reached values up to ~ 2.9 and ~ 3.6 for normal and oblique wave incidence, respectively (Fig. 11). The contribution of IG energy was found to be more pronounced in evaluation points near the south antinode which is common in multiple resonant modes, i.e. evaluation points 9–15 (Fig. 8). In contrary, for normal incidence, the smallest $q_{HF,SWL}/q_{HF-IG,SWL}$ ratios were found for evaluation locations 1–3 due to low IG energy relative to the total, and for evaluation locations 16–18 due to relatively higher freeboards. These observations concur with the notion that IG contribution to wave overtopping is highest when the IG/total energy ratio is the highest and freeboard is the lowest.

Approach A also allowed us to examine the contribution of harbour resonance to wave overtopping by modelling the IG energy as a (stochastic) freeboard adjustment of the vertical walls surrounding the western basin. Time series of IG waves extracted from the numerical simulation at the toe of each evaluation points were translated to freeboard adjustment to obtain time series of overtopping rate $q_{HF,ADJ}$. FFT analysis of $q_{HF,ADJ}$ revealed which resonant modes contribute the

most to wave overtopping in each evaluation location (Fig. 12). Obtaining the mean value $\bar{q}_{HF,ADJ}$ and comparing it to $q_{HF,SWL}$ provided an approximation for the total contribution of harbour resonance to wave overtopping rates. $\bar{q}_{HF,ADJ}$ is driven by the non-linear behaviour of the overtopping equations to changes in the freeboard and the ratio $\bar{q}_{HF,ADJ}/q_{HF,SWL}$ was found to be largest in evaluation locations with the lowest SWL freeboard.

In comparison with $q_{HF-IG,SWL}$ for which IG energy is included in the spectral parameters used with the EurOtop formulae ($H_{m0}, T_{m-1,0}$), $\bar{q}_{HF,ADJ}$ rates were lower for most evaluation points. The two approaches are fundamentally different. For impulsive conditions, $q_{HF-IG,SWL}$ accounts for the influence of IG in spectral period $T_{m-1,0}$, whereas $\bar{q}_{HF,ADJ}$ treats all IG fluctuations ($f < 0.04$ Hz) as being long-enough to be considered a change in the SWL. The IG limit of 0.04 Hz was used in this application because this frequency range is typically the range in which harbour resonant frequencies are detected, however, its use as an upper limit for considering long waves as a change to the SWL is rather arbitrary. The proposed methodology of evaluating the influence of harbour resonance in wave overtopping rates needs to be validated through field measurements of wave overtopping at the harbour docks or through well-controlled laboratory experiments for vertical walls with significant influence from a shallow foreshore. This is particularly important as rising sea levels due to climate change will increase overtopping volumes, and likely the frequency of extreme storms.

7. Glossary

f : frequency

f_n : resonant frequency (eigenfrequency)

$S(f)$: spectral energy density

Δf : field spectral energy density frequency step

df : frequency step of the input spectrum used with the numerical model

T_{FSE} : total duration of field time series

m_n : spectral moments

H_{m0} : spectral significant wave height

T_p : peak wave period

$T_{m-1,0}$: spectral wave period computed using the m_{-1} and m_0 spectral moments

T_n : resonant period (eigenperiod)

$L_{m-1,0}$: wavelength corresponding to $T_{m-1,0}$

$s_{m-1,0}$: wave steepness corresponding to $L_{m-1,0}$

$H_{1/3}$: zero-down crossing significant wave height

$T_{1/3}$: zero-down crossing significant wave period

H_{max} : zero-down crossing maximum wave height

g : gravitational acceleration

MWL : mean water level

h : depth at the toe of the structure

q : mean overtopping rate

R_c : crest freeboard

γ_β : reduction factor for oblique incidence

β : wave incident angle relative to the structure orientation

k_β : obliquity factor

ϕ : mean incident wave direction

η_{IG} : free surface elevation in the infragravity frequency range ($f <$ 0.04 Hz) extracted from the numerical simulation at the toe of the structures

$R_{c,SWL}$: crest freeboard relative to still water level

$R_{c,IG}$: adjusted freeboard time series ($R_{c,SWL} - \eta_{IG}$)

$q_{HF,SWL}$: mean overtopping rate obtained from the higher frequency range ($f > 0.04$ Hz) of the incident wave spectrum and $R_{c,SWL}$

$q_{HF,ADJ}$: time series of overtopping discharge obtained from the higher frequency range of the incident wave spectrum and (time series) $R_{c,IG}$

$\bar{q}_{HF,ADJ}$: mean overtopping rate obtained by averaging time series $q_{HF,ADJ}$

$q_{HF-IG,SWL}$: mean overtopping rate obtained from the full frequency range of the incident wave spectrum and $R_{c,SWL}$

CRediT authorship contribution statement

Nikolaos Maravelakis: Conceptualization, Methodology, Software, Visualization, Formal analysis, Investigation, Writing – original draft. **Nikos Kalligeris:** Conceptualization, Methodology, Software, Visualization, Writing – original draft. **Patrick J. Lynett:** Conceptualization, Methodology, Software, Resources, Supervision, Writing – review & editing. **Vassilios L. Skanavis:** Investigation. **Costas E. Synolakis:** Conceptualization, Supervision, Project administration, Funding acquisition, Writing – review & editing.

Declaration of competing interest

The authors declare that they have no known competing financial interests or personal relationships that could have appeared to influence the work reported in this paper.

Acknowledgements

This work was financially supported by the Municipal Port Fund of Chania (Greece) through the research assignment “Marina placement, wave conditions of the Venetian harbour, and coastline evolution of Chania municipality coastal front”. The contribution of Yannis Dapolas and diving schools of Artemis Cheiladakis and Nikos Giannoulakis was essential in the collection of field data. We thank the Chania Sailing Club for providing their boat and facilities for many phases of our field work.

References

Abdelhafez, M.A., Ellingwood, B., Mahmoud, H., 2021. Vulnerability of seaports to hurricanes and sea level rise in a changing climate: A case study for Mobile, AL. Coast. Eng. 103884. http://dx.doi.org/10.1016/j.coastaleng.2021.103884.

Almar, R., Ranasinghe, R., Bergsma, E.W.J., Diaz, H., Melet, A., Papa, F., Vousdoukas, M., Athanasiou, P., Dada, O., Almeida, L.P., Kestenare, E., 2021. A global analysis of extreme water levels with implications for potential coastal overtopping. Nature Commun. 12, 3775. http://dx.doi.org/10.1038/s41467-021-24008-9.

André, G., Bellafont, F., Leckler, F., Morichon, D., 2021. Predicting seiche hazard for coastal harbours along the northern and western coasts of France. Nat. Hazards 106 (1), 1065–1086. http://dx.doi.org/10.1007/s11069-021-04509-y.

Asariotis, R., Benamara, H., Mohos-Naray, V., 2018. Port Industry Survey on Climate Change Impacts and Adaptation. Retrieved from United nations Conference on Trade and Development, https://unctad.org/en/PublicationsLibrary/ser-rp-2017d18_en.pdf.

Baldock, T., Huntley, D., 2002. Long–wave forcing by the breaking of random gravity waves on a beach. Proc. R. Soc. Lond. Ser. A Math. Phys. Eng. Sci. 458 (2025), 2177–2201. http://dx.doi.org/10.1098/rspa.2002.0962.

Battjes, J., Bakkenes, H., Janssen, T., van Dongeren, A., 2004. Shoaling of subharmonic gravity waves. J. Geophys. Res. Oceans 109 (C2), http://dx.doi.org/10.1029/2003JC001863.

Baumann, J., Chaumillon, E., Bertin, X., Schneider, J.-L., Guillot, B., Schmutz, M., 2017. Importance of infragravity waves for the generation of washover deposits. Mar. Geol. 391, 20–35. http://dx.doi.org/10.1016/j.margeo.2017.07.013.

Bellotti, G., 2007. Transient response of harbours to long waves under resonance conditions. Coast. Eng. 54 (9), 680–693. http://dx.doi.org/10.1016/j.coastaleng.2007.02.002.

Bellotti, G., Briganti, R., Beltrami, G.M., Franco, L., 2012. Modal analysis of semi-enclosed basins. Coast. Eng. 64, 16–25. http://dx.doi.org/10.1016/j.coastaleng.2012.02.002.

Bellotti, G., Franco, L., 2011. Measurement of long waves at the harbor of Marina di Carrara, Italy. Ocean Dyn. 61 (12), 2051–2059. http://dx.doi.org/10.1007/s10236-011-0468-6.

Bowers, E., 1977. Harbour resonance due to set-down beneath wave groups. J. Fluid Mech. 79 (1), 71–92. http://dx.doi.org/10.1017/S0022112077000044.

Camus, P., Tomás, A., Díaz-Hernández, G., Rodríguez, B., Izaguirre, C., Losada, I., 2019. Probabilistic assessment of port operation downtimes under climate change. Coast. Eng. 147, 12–24. http://dx.doi.org/10.1016/j.coastaleng.2019.01.007.

Chini, N., Stansby, P., 2012. Extreme values of coastal wave overtopping accounting for climate change and sea level rise. Coast. Eng. 65, 27–37. http://dx.doi.org/10.1016/j.coastaleng.2012.02.009.

Cuomo, G., Guza, R., 2017. Infragravity seiches in a small harbor. J. Waterw. Port Coast. Ocean Eng. 143 (5), 04017032. http://dx.doi.org/10.1061/(ASCE)WW.1943-5460.0000392.

De Girolamo, P., 1996. An experiment on harbour resonance induced by incident regular waves and irregular short waves. Coast. Eng. 27 (1–2), 47–66. http://dx.doi.org/10.1016/0378-3839(95)00039-9.

Dong, G., Zheng, Z., Gao, J., Ma, X., Dong, Y., Wu, H., 2020a. Experimental investigation on special modes with narrow amplification diagrams in harbor oscillations. Coast. Eng. 159, 103720. http://dx.doi.org/10.1016/j.coastaleng.2020.103720.

Dong, G., Zheng, Z., Ma, X., Huang, X., 2020b. Characteristics of low-frequency oscillations in the Hambantota Port during the southwest monsoon. Ocean Eng. 208, 107408. http://dx.doi.org/10.1016/j.oceaneng.2020.107408.

Douyere, Y.M., 2003. Analysis of Harbor Oscillation with a Boussinesq Model (Ph.D. thesis). University of Hawaii at Manoa, http://hdl.handle.net/10125/6998.

Dusseljee, D., Klopman, G., Van Vledder, G.P., Riezebos, H.J., 2014. Impact of harbor navigation channels on waves: A numerical modelling guideline. In: Proceedings of 34th International Conference on Coastal Engineering, Seoul, Korea, 15-20 June 2014, http://dx.doi.org/10.9753/icce.v34.waves.58.

EurOtop, 2018. Manual on Wave Overtopping of Sea Defences and Related Structures. An Overtopping Manual Largely Based on European Research, but for Worldwide Application, second ed. www.overtopping-manual.com.

Gallien, T., Sanders, B., Flick, R., 2014. Urban coastal flood prediction: Integrating wave overtopping, flood defenses and drainage. Coast. Eng. 91, 18–28. http://dx.doi.org/10.1016/j.coastaleng.2014.04.007.

Gao, J., Ji, C., Gaidai, O., Liu, Y., 2016. Numerical study of infragravity waves amplification during harbor resonance. Ocean Eng. 116, 90–100. http://dx.doi.org/10.1016/j.oceaneng.2016.02.032.

Gao, J., Ma, X., Zang, J., Dong, G., Ma, X., Zhu, Y., Zhou, L., 2020. Numerical investigation of harbor oscillations induced by focused transient wave groups. Coast. Eng. 158, 103670. http://dx.doi.org/10.1016/j.coastaleng.2020.103670.

Gensen, M., 2017. Wave Overtopping in Harbour Areas (MSc Thesis). Delft University of Technology, Delft, The Netherlands, http://resolver.tudelft.nl/uuid:70821fb8-7df3-48e9-8058-0e10cbb97492.

Gierlevsen, T., Hebsgaard, M., Kirkegaard, J., 2001. Wave disturbance modelling in the Port of Sines, Portugal–with special emphasis on long period oscillations. In: Proceedings International Conference on Port and Maritime R&D and Technology, Singapore, 29-13 October 2001.

Goda, Y., 1988. Statistical variability of sea state parameters as a function of wave spectrum. Coast. Eng. Japan 31 (1), 39–52. http://dx.doi.org/10.1080/05785634.1988.11924482.

Goda, Y., 2010. Random Seas and Design of Maritime Structures, Vol. 33. World Scientific Publishing Company, http://dx.doi.org/10.1142/7425.

Guerrini, M., Bellotti, G., Fan, Y., Franco, L., 2014. Numerical modelling of long waves amplification at Marina di Carrara Harbour. Appl. Ocean Res. 48, 322–330. http://dx.doi.org/10.1016/j.apor.2014.10.002.

Guza, R., Thornton, E.B., 1982. Swash oscillations on a natural beach. J. Geophys. Res. Oceans 87 (C1), 483–491. http://dx.doi.org/10.1029/JC087iC01p00483.

Harkins, G.S., Briggs, M.J., 1995. Resonant forcing of harbors by infragravity waves. In: Coastal Engineering 1994. pp. 806–820. http://dx.doi.org/10.1061/9780784400890.060.

Hashimoto, N., Nakagawa, Y., Nagai, T., Ito, K., 1997. Modification of extended maximum entropy principle method (EMEP) for estimating directional spectrum in incident and reflected wave field. In: Proceedings of the 1997 16th International Conference on Offshore Mechanics and Arctic Engineering. Part 1-B (of 6).

Hofland, B., Chen, X., Altomare, C., Oosterlo, P., 2017. Prediction formula for the spectral wave period Tm-1, 0 on mildly sloping shallow foreshores. Coast. Eng. 123, 21–28. http://dx.doi.org/10.1016/j.coastaleng.2017.02.005.

Holman, R., Huntley, D., Bowen, A., 1978. Infragravity waves in storm conditions. In: Coastal Engineering 1978. pp. 268–284. http://dx.doi.org/10.9753/icce.v16.13.

Jeong, W., Chae, J., Park, W., Jung, K., 1997. Field measurements and numerical modeling of harbor oscillations during storm waves. In: Coastal Engineering 1996. pp. 1268–1279. http://dx.doi.org/10.1061/9780784402429.099.

Kennedy, A.B., Chen, Q., Kirby, J.T., Dalrymple, R.A., 2000. Boussinesq modeling of wave transformation, breaking, and runup. I: 1D. J. Waterw. Port Coast. Ocean Eng. 126 (1), 39–47. http://dx.doi.org/10.1061/(ASCE)0733-950X(2000)126:1(39).

Kim, D.-H., Lynett, P.J., Socolofsky, S.A., 2009. A depth-integrated model for weakly dispersive, turbulent, and rotational fluid flows. Ocean Model. 27 (3–4), 198–214. http://dx.doi.org/10.1016/j.ocemod.2009.01.005.

Kirby, J., Wei, G., Chen, Q., Kennedy, A., Dalrymple, R., 1998. FUNWAVE 1.0: Fully Nonlinear Boussinesq Wave Model Documentation and User's Manual. Center for Applied Coastal Research, University of Delaware, http://resolver.tudelft.nl/uuid:d79bba08-8d35-47e2-b901-881c86985ce4.

Kofoed-Hansen, H., Kerper, D.R., Sørensen, O.R., Kirkegaard, J., 2005. Simulation of long wave agitation in ports and harbours using a time-domain Boussinesq model. In: Proceedings of the Fifth International Symposium on Ocean Wave Measurement and Analysis (WAVES), Madrid, Spain.

Kofoed-Hansen, H., Sloth, P., Sørensen, O.R., Fuchs, J., 2001. Combined numerical and physical modelling of seiching in exposed new marina. In: Coastal Engineering 2000. pp. 3600–3614. http://dx.doi.org/10.1061/40549(276)281.

Kwak, M.S., mu Jeong, W., Kobayashi, N., 2020. A case study on harbor oscillations by infragravity waves. Coast. Eng. Proc. (36v), 33. http://dx.doi.org/10.9753/icce.v36v.papers.33.

Leys, V., Fernandez, V., Kolijn, D., 2018. Resonant oscillations in small craft harbours: observations and mitigation examples from Atlantic Canada. Coast. Eng. Proc. (36), 62. http://dx.doi.org/10.9753/icce.v36.papers.62.

Longuet-Higgins, M., Stewart, R., 1962. Radiation stress and mass transport in gravity waves, with application to 'surf beats'. J. Fluid Mech. 13 (4), 481–504. http://dx.doi.org/10.1017/S0022112062000877.

Longuet-Higgins, M.S., Stewart, R., 1964. Radiation stresses in water waves; a physical discussion, with applications. Deep Sea Res. Oceanogr. Abstr. 11 (4), 529–562. http://dx.doi.org/10.1016/0011-7471(64)90001-4.

López, M., Iglesias, G., 2013. Artificial intelligence for estimating infragravity energy in a harbour. Ocean Eng. 57, 56–63. http://dx.doi.org/10.1016/j.oceaneng.2012.08.009.

López, M., Iglesias, G., Kobayashi, N., 2012. Long period oscillations and tidal level in the Port of Ferrol. Appl. Ocean Res. 38, 126–134. http://dx.doi.org/10.1016/j.apor.2012.07.006.

Løvholt, F., Lynett, P., Pedersen, G., 2013. Simulating run-up on steep slopes with operational Boussinesq models; capabilities, spurious effects and instabilities. Nonlinear Process. Geophys. 20 (3), 379–395. http://dx.doi.org/10.5194/npg-20-379-2013.

Lynett, P.J., 2002. A Multi-Layer Approach to Modeling Generation, Propagation, and Interaction of Water Waves (Ph.D. thesis). Cornell University, http://coastal.usc.edu/plynett/publications/PLynett_thesis.pdf.

Lynett, P., Liu, P.-F., Sitanggang, K., Kim, D.-H., 2008. Modeling wave generation, evolution, and interaction with depth integrated, dispersive wave equations: COULWAVE code manual. In: Cornell University Long and Intermediate Wave Modeling Package V2.

Lynett, P.J., Wu, T.-R., Liu, P.L.-F., 2002. Modeling wave runup with depth-integrated equations. Coast. Eng. 46 (2), 89–107. http://dx.doi.org/10.1016/S0378-3839(02)00043-1.

Ma, X., Zheng, Z., Gao, J., Wu, H., Dong, Y., Dong, G., 2021. Experimental investigation of transient harbor resonance induced by solitary waves. Ocean Eng. 230, 109044. http://dx.doi.org/10.1016/j.oceaneng.2021.109044.

Maravelakis, N., Kalligeris, N., Lynett, P., Synolakis, C., 2016. Case study of small harbor excitation under storm conditions. In: Ports 2016. pp. 647–656. http://dx.doi.org/10.1061/9780784479902.065.

McCall, R., Masselink, G., Poate, T., Roelvink, J., Almeida, L., Davidson, M., Russell, P., 2014. Modelling storm hydrodynamics on gravel beaches with XBeach-G. Coast. Eng. 91, 231–250. http://dx.doi.org/10.1016/j.coastaleng.2014.06.007.

McComb, P., Gorman, R., Goring, D., 2005. Forecasting infragravity wave energy within a harbour. In: Proceedings of Waves 2005 Conference, Madrid. pp. 3–7.

McComb, P., Johnson, D., Beamsley, B., 2009. Numerical study of options to reduce swell and long wave penetration at port Geraldton. In: Coasts and Ports 2009:In a Dynamic Environment. Engineers Australia, pp. 490–496.

Mei, C.C., Agnon, Y., 1989. Long-period oscillations in a harbour induced by incident short waves. J. Fluid Mech. 208, 595–608. http://dx.doi.org/10.1017/S0022112089002958.

Mitsuyasu, H., Tasai, F., Suhara, T., Mizuno, S., Ohkusu, M., Honda, T., Rikiishi, K., 1975. Observations of the directional spectrum of ocean waves using a cloverleaf buoy. J. Phys. Oceanogr. 5 (4), 750–760. http://dx.doi.org/10.1175/1520-0485(1975)005<0750:OOTDSO>2.0.CO;2.

Modesto, D., Ye, B., Zlotnik, S., Huerta, A., 2020. Fast solution of elliptic harbor agitation problems under frequency-direction input spectra by model order reduction and NURBS-enhanced FEM. Coast. Eng. 156, 103618. http://dx.doi.org/10.1016/j.coastaleng.2019.103618.

Morison, M.L., Imberger, J., 1992. Water-level oscillations in Esperance Harbour. J. Waterw. Port Coast. Ocean Eng. 118 (4), 352–367. http://dx.doi.org/10.1061/(ASCE)0733-950X(1992)118:4(352).

Nakamura, S., Katoh, K., 1993. Generation of infragravity waves in breaking process of wave groups. In: Coastal Engineering 1992. pp. 990–1003. http://dx.doi.org/10.1061/9780872629332.074.

Nicolai, R., Van Vuren, S., Pleijter, G., Huizinga, J., Koks, E., De Moel, H., 2016. Pilot Waterveiligheid Botlek; Kwantitatieve Analyse Overstromingsrisico's. Technical Report.

Nortek, 2018. The Comprehensive Manual. p. 153, URL: https://support.nortekgroup.com/hc/en-us/categories/360001447411-Manuals.

Nortek, 2021. AWAC 600kHz. URL: www.nortekgroup.com/products/awac-600-khz.

Nwogu, O.G., 2001. Time domain simulation of long period oscillations in harbors. In: Coastal Engineering 2000. pp. 3643–3654. http://dx.doi.org/10.1061/40549(276)284.

Okihiro, M., Guza, R., 1996. Observations of seiche forcing and amplification in three small harbors. J. Waterw. Port Coast. Ocean Eng. 122 (5), 232–238. http://dx.doi.org/10.1061/(ASCE)0733-950X(1996)122:5(232).

Okihiro, M., Guza, R., Seymour, R., 1993. Excitation of seiche observed in a small harbor. J. Geophys. Res. Oceans 98 (C10), 18201–18211. http://dx.doi.org/10.1029/93JC01760.

Oosterlo, P., McCall, R.T., Vuik, V., Hofland, B., Van der Meer, J.W., Jonkman, S.N., 2018. Probabilistic assessment of overtopping of sea dikes with foreshores including infragravity waves and morphological changes: Westkapelle case study. J. Mar. Sci. Eng. 6 (2), 48. http://dx.doi.org/10.3390/jmse6020048.

Papadopoulos, A., 2009. Determination of Sea Level through Field Measurements and Satellite Altimetry (In Greek) (Ph.D. thesis). Technical University of Crete, Greece.

Pawlowicz, R., Beardsley, B., Lentz, S., 2002. Classical tidal harmonic analysis including error estimates in MATLAB using T_TIDE. Comput. Geosci. 28 (8), 929–937. http://dx.doi.org/10.1016/S0098-3004(02)00013-4.

Rabinovich, A.B., 2009. Seiches and harbor oscillations. In: Handbook of Coastal and Ocean Engineering. World Scientific, pp. 193–236. http://dx.doi.org/10.1142/9789812819307_0009.

Raubenheimer, B., Guza, R., Elgar, S., 1996. Wave transformation across the inner surf zone. J. Geophys. Res. Oceans 101 (C11), 25589–25597. http://dx.doi.org/10.1029/96JC02433.

Ruessink, B., Kleinhans, M., Van den Beukel, P., 1998. Observations of swash under highly dissipative conditions. J. Geophys. Res. Oceans 103 (C2), 3111–3118. http://dx.doi.org/10.1029/97JC02791.

Sierra, J., Genius, A., Lionello, P., Mestres, M., Mösso, C., Marzo, L., 2017. Modelling the impact of climate change on harbour operability: The Barcelona port case study. Ocean Eng. 141, 64–78. http://dx.doi.org/10.1016/j.oceaneng.2017.06.002.

Synolakis, C., Kânoğlu, U., 2015. The Fukushima accident was preventable. Phil. Trans. R. Soc. A 373 (2053), 20140379. http://dx.doi.org/10.1098/rsta.2014.0379.

Thotagamuwage, D.T., Pattiaratchi, C.B., 2014. Observations of infragravity period oscillations in a small marina. Ocean Eng. 88, 435–445. http://dx.doi.org/10.1016/j.oceaneng.2014.07.003.

Troch, C., Terblanche, L., Henning, H., 2021. Modelling and measurement of low-frequency surge motion associated with extreme storm conditions in the Port of Cape Town. Appl. Ocean Res. 106, 102452. http://dx.doi.org/10.1016/j.apor.2020.102452.

Tsimplis, M., 1994. Tidal oscillations in the Aegean and Ionian Seas. Estuar. Coast. Shelf Sci. 39 (2), 201–208. http://dx.doi.org/10.1006/ecss.1994.1058.

Tsimplis, M., Proctor, R., Flather, R., 1995. A two-dimensional tidal model for the Mediterranean Sea. J. Geophys. Res. Oceans 100 (C8), 16223–16239. http://dx.doi.org/10.1029/95JC01671.

Vitousek, S., Barnard, P.L., Fletcher, C.H., Frazer, N., Erikson, L., Storlazzi, C.D., 2017. Doubling of coastal flooding frequency within decades due to sea-level rise. Sci. Rep. 7 (1), 1–9. http://dx.doi.org/10.1038/s41598-017-01362-7.

Vousdoukas, M.I., Mentaschi, L., Voukouvalas, E., Verlaan, M., Jevrejeva, S., Jackson, L.P., Feyen, L., 2018. Global probabilistic projections of extreme sea levels show intensification of coastal flood hazard. Nature Commun. 9 (1), 1–12. http://dx.doi.org/10.1038/s41467-018-04692-w.

Wong, P., Losada, I., Gattuso, J., Hinkel, J., Khattabi, A., McInnes, K., Saito, Y., Sallenger, A., 2014. Coastal systems and low-lying areas. In: Climate Change 2014: Impacts, Adaptation, and Vulnerability. Part A: Global and Sectoral Aspects. Contribution of Working Group II to the Fifth Assessment Report of the Intergovernmental Panel on Climate Change. Cambridge University Press, Cambridge, United Kingdom and New York, NY, USA, pp. 361–409, https://www.ipcc.ch/site/assets/uploads/2018/02/WGIIAR5-Chap5_FINAL.pdf.

Wu, J.-K., Liu, P.L.-F., 1990. Harbour excitations by incident wave groups. J. Fluid Mech. 217, 595–613. http://dx.doi.org/10.1017/S0022112090000866.

Xie, D., Zou, Q.-P., Mignone, A., MacRae, J., 2019. Coastal flooding from wave overtopping and sea level rise adaptation in the northeastern USA. Coast. Eng. 150, 39–58. http://dx.doi.org/10.1016/j.coastaleng.2019.02.001.

Zheng, Z., Ma, X., Ma, Y., Dong, G., 2020. Wave estimation within a port using a fully nonlinear Boussinesq wave model and artificial neural networks. Ocean Eng. 216, 108073. http://dx.doi.org/10.1016/j.oceaneng.2020.108073.

Zheng, Z., Ma, X., Ma, Y., Perlin, M., Dong, G., 2021. Numerical investigation of seismic-induced harbor oscillations. Coast. Eng. 165, 103838. http://dx.doi.org/10.1016/j.coastaleng.2020.103838.

Zwamborn, J., Grieve, G., 1975. Wave attenuation and concentration associated with harbour approach channels. In: Coastal Engineering 1974. pp. 2068–2085. http://dx.doi.org/10.9753/icce.v14.120.